JWST sighting of decametre main-belt asteroids and view on meteorite sources

Burdanov, A.Y.; Wit, J. de; Brož, M.; Müller, T.G.; Hoffmann, T.; Ferrais, M.; ... ; Zieba, S.

Article

JWST sighting of decametre main-belt asteroids and view on meteorite sources

https://doi.org/10.1038/s41586-024-08480-z

Received: 29 July 2024

Accepted: 13 November 2024

Published online: 9 December 2024

Check for updates

Artem Y. Burdanov[1,16], Julien de Wit[1,16]✉, Miroslav Brož[2], Thomas G. Müller[3], Tobias Hoffmann[4], Marin Ferrais[5], Marco Micheli[6], Emmanuel Jehin[7], Daniel Parrott[8], Samantha N. Hasler[1], Richard P. Binzel[1], Elsa Ducrot[9], Laura Kreidberg[10], Michaël Gillon[11], Thomas P. Greene[12], Will M. Grundy[13], Theodore Kareta[13], Pierre-Olivier Lagage[9], Nicholas Moskovitz[13], Audrey Thirouin[13], Cristina A. Thomas[14] & Sebastian Zieba[10,15]

Asteroid discoveries are essential for planetary-defence efforts aiming to prevent impacts with Earth[1], including the more frequent[2] megaton explosions from decametre impactors[3–6]. Although large asteroids (≥100 kilometres) have remained in the main belt since their formation[7], small asteroids are commonly transported to the near-Earth object (NEO) population[8,9]. However, owing to the lack of direct observational constraints, their size–frequency distribution (SFD)—which informs our understanding of the NEOs and the delivery of meteorite samples to Earth—varies substantially among models[10–14]. Here we report 138 detections of some of the smallest asteroids (≥10 metres) ever observed in the main belt, which were enabled by JWST's infrared capabilities covering the emission peaks of the asteroids[15] and synthetic tracking techniques[16–18]. Despite small orbital arcs, we constrain the distances and phase angles of the objects using known asteroids as proxies, allowing us to derive sizes through radiometric techniques. Their SFD shows a break at about 100 metres (debiased cumulative slopes of $q = -2.66 \pm 0.60$ and -0.97 ± 0.14 for diameters smaller and larger than roughly 100 metres, respectively), suggestive of a population driven by collisional cascade. These asteroids were sampled from several asteroid families—most probably Nysa, Polana and Massalia—according to the geometry of pointings considered here. Through further long-stare infrared observations, JWST is poised to serendipitously detect thousands of decametre-scale asteroids across the sky, examining individual asteroid families[19] and the source regions of meteorites[13,14] 'in situ'.

Asteroids are discovered by their motion relative to the background stars. This observed motion results from the actual orbital movement of asteroids combined with motion induced by Earth's (and/or a satellite's) parallactic movement. Although most asteroid-search projects detect objects in single images (exposures) and link their motion across several images, this method may miss fainter objects that are not visible on an individual image. To address this, the 'shift-and-stack' technique, developed in the 1990s, enhances the signal-to-noise ratio (SNR) by combining several images into one 'stack' image[16,20,21]. This method involves predicting the motion of the asteroid, shifting image pixels accordingly and then combining the images (Fig. 1). Synthetic tracking, an extension of the shift-and-stack technique, does not rely on previous knowledge of the motion of an asteroid but instead performs a fully 'blind' search by testing a series of possible shifts[17,22,23] (that is, velocity vectors). However, the computational intensity of this method posed a bottleneck until the widespread availability of graphics processing units (GPUs). The subsequent use of GPU-based synthetic tracking increases the scientific return of monitory campaigns, such as exoplanet transit-search surveys, by recovering serendipitous asteroid detections[18,24].

Most of the known asteroids have been discovered by ground-based surveys at visible wavelengths. The full spectral energy distributions of asteroids are a combination of reflected sunlight (driven by the albedo of the object) and thermal emission, with the central wavelengths of the thermal peak ranging between 5 and 20 μm for objects between 1 and 10 AU (Fig. 2). With a sensitivity in that wavelength range and a large aperture, JWST is ideal for detecting the thermal emission of asteroids and revealing the smallest main-belt asteroids (MBAs)[15]. Such observations combined with orbital information can yield accurate radius estimates, which are less affected by degeneracy with the albedo than those from visible-light observations[25–27]. Indeed, the visible-light detection of a typical MBA with known orbit can be explained by an object

[1]Department of Earth, Atmospheric, and Planetary Sciences, Massachusetts Institute of Technology, Cambridge, MA, USA. [2]Faculty of Mathematics and Physics, Astronomical Institute of Charles University, Prague, Czech Republic. [3]Max-Planck-Institut für extraterrestrische Physik, Garching, Germany. [4]Department of Medical Physics and Acoustics, Carl von Ossietzky University of Oldenburg, Oldenburg, Germany. [5]Florida Space Institute, University of Central Florida, Orlando, FL, USA. [6]ESA PDO NEO Coordination Centre, Frascati, Italy. [7]Space sciences, Technologies and Astrophysics Research (STAR) Institute, University of Liège, Liège, Belgium. [8]Tycho Tracker, Parrott's Studio, LLC, Oklahoma City, OK, USA. [9]Université Paris-Saclay, Université Paris Cité, CEA, CNRS, AIM, Gif-sur-Yvette, France. [10]Max-Planck-Institut für Astronomie, Heidelberg, Germany. [11]Astrobiology Research Unit, University of Liège, Liège, Belgium. [12]Space Science and Astrobiology Division, NASA Ames Research Center, Moffett Field, CA, USA. [13]Lowell Observatory, Flagstaff, AZ, USA. [14]Department of Astronomy and Planetary Science, Northern Arizona University, Flagstaff, AZ, USA. [15]Leiden Observatory, Leiden University, Leiden, The Netherlands. [16]These authors contributed equally: Artem Y. Burdanov, Julien de Wit. ✉e-mail: jdewit@mit.edu

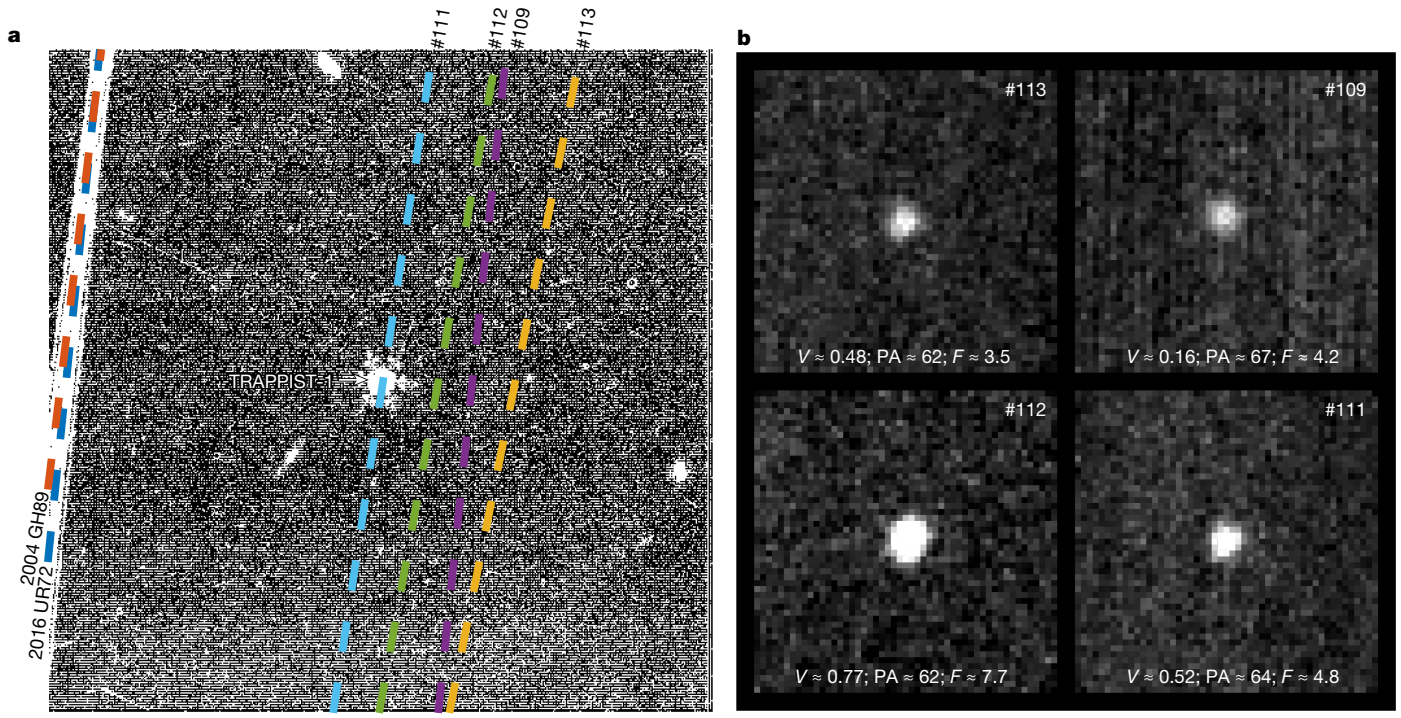

Fig. 1 | Basics of a blind search for asteroids using synthetic tracking. **a**, Average stack of exposures 4,000 to 4,500 from PID 3077 centred on the ultracool star TRAPPIST-1, revealing two known bright asteroids (2004 GH89 and 2016 UR72) crossing the left side of the FoV (field of view). Being bright, they are detectable on individual exposures, leading to a trail on the stacked exposure. The other dashed lines refer to the paths of four unknown asteroids crossing the FoV at the same time but only detectable in stacked exposures that are first shifted along their respective paths, which are identified through a blind search by means of the shift-and-stack technique. **b**, Shifted-and-stacked exposures centred on four new asteroids (#113, #109, #112 and #111) with their speed (V, in arcsec min^{-1}), position angle (PA, in °) and flux (F, in μJy). All of the properties of the 138 new asteroids are reported in Supplementary Table 1 and their shifted-and-stacked exposures in Supplementary Fig. 1.

with a small size with high albedo or a large size with low albedo. For the wide range of albedos from 3 to 40%, the corresponding sizes can vary by a factor of 3–4. By contrast, a thermal infrared measurement close to the thermal peak of the object constrains the size of the object to within about 10–20% (Methods).

JWST's potential and decametre delivering

JWST observing programmes conducted with no dithering are especially suitable for synthetic tracking, as all exposures from one visit can be shifted and stacked. This makes JWST sensitive to small infrared fluxes from moving objects in a field of view (FoV) and enhances its capability to detect faint asteroids. Such a dithering-free long-stare mode was used to observe the TRAPPIST-1 star (located 0.6° from the ecliptic) with the MIRI instrument[28] at 15 μm as part of several programmes aimed at characterizing the TRAPPIST-1 exoplanetary system through measurements of the inner planets' dayside emission (programme IDs (PIDs) 1177 and 2304, with Greene and Kreidberg as PI, respectively) and their combined thermal phase curve (PID 3077, principal investigator M.G.). In total, JWST observed the TRAPPIST-1 star for 93.5 h during 11 visits in 2022–2023. After applying our GPU-based framework for detecting asteroids in targeted exoplanet surveys[18,24], we were able to detect eight known and 138 unknown asteroids that happened to serendipitously cross the MIRI FoV of 56.3″ × 56.3″ or 112″ × 113″ (depending on the particular observing programme). The known objects are MBAs with fluxes between 100 and 1,700 μJy and diameters (D) between 200 and 2,500 m (Extended Data Table 1).

The 138 new detections could not be attributed to any known asteroids, for which we searched for previously discovered objects positioned closer than 1′ from each detection (Methods). Infrared fluxes of these new objects range from 0.5 to 600 μJy, with a detection/sensitivity threshold at about 0.5 μJy (Methods and Extended Data Fig. 1). Our detections spend from 30 min to 8 h in the MIRI FoV. Even in the case of the longest observing arc of 8 h, orbits of different dynamical classes can fit the data well and are statistically indistinguishable. We thus used ensembles of known objects that were predicted to be in a 6° × 2° area around the TRAPPIST-1 star at the time of detection of an unknown asteroid as proxies to derive posterior probability distributions on the distance from JWST to each unknown asteroid (see example in Extended Data Fig. 2). This methodology yielded the distance with a typical uncertainty of about 0.2 AU and adequately returned the distance of the eight known asteroids (Methods and Extended Data Fig. 3). We estimated distances from JWST to unknown asteroids to be from 0.9 to 3.0 AU, placing them primarily in the main asteroid belt, with diameters ranging from 10 to 500 m (Fig. 3 and Methods). Among them, six seem associated with the population of NEOs (marked as 'NEOs?' in Fig. 3) and one with the population of trojans (Methods and Extended Data Table 2). The detection/sensitivity threshold at about 0.5 μJy starts at roughly 1.5 μJy and translates into an observational bias emerging in the 20–40-m-diameter regime with a sharp cutoff by about 10 m (Extended Data Fig. 1).

Population statistics and possible origins

The SFD of our asteroid detections is unusually shallow at sizes larger than about 100 m, corresponding to a population depleted by collisions (Fig. 4). It can be described by a power law, $N(>D) = CD^q$, with the exponent $q = -0.97 \pm 0.14$. This exponent is derived from the debiased SFD, that is, the observed SFD corrected for the size-dependent recovery rate and the non-negligible uncertainties of individual size estimates (Methods). On the other hand, the observed SFD is much steeper below 100 m, with a debiased exponent $q = -2.66 \pm 0.60$,

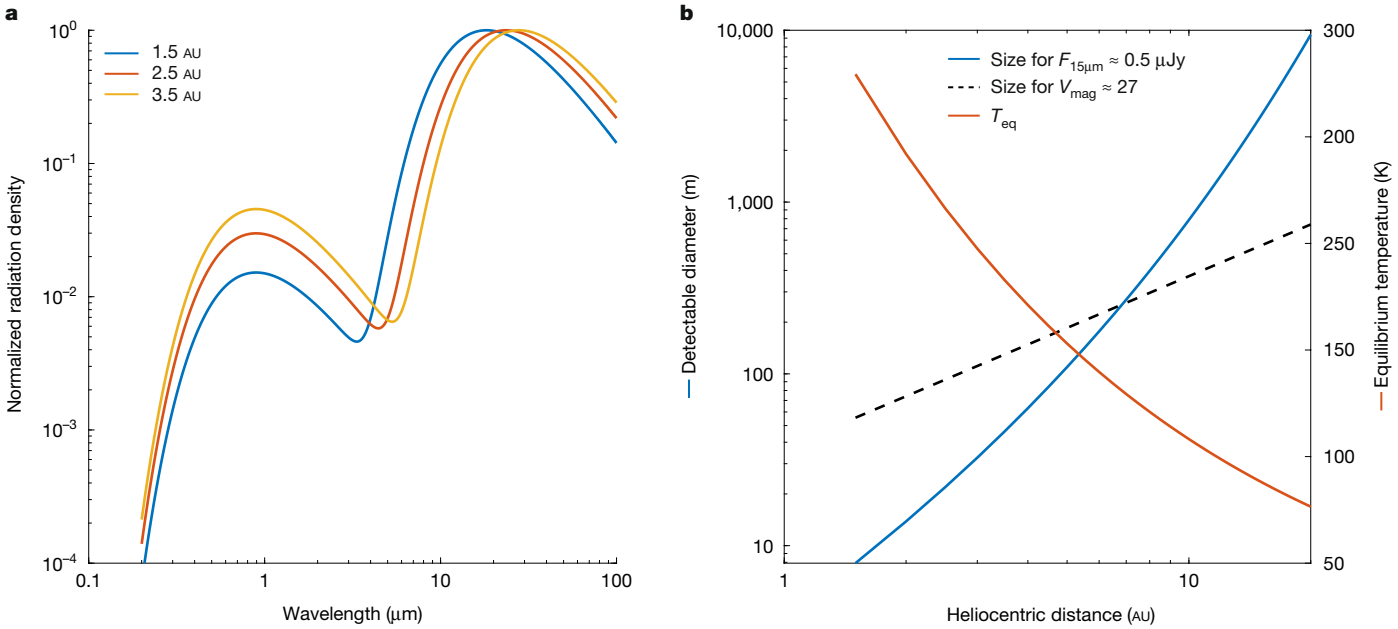

Fig. 2 | JWST's far-infrared window into the MBA population. a, Radiation density (Jy) normalized to the peak emission for 0.1-albedo asteroids with a heliocentric distance of 1.5 AU (blue), 2.5 AU (red) and 3.5 AU (yellow) showcasing the favourable infrared-to-visible flux ratio. **b**, Minimum size of an asteroid detectable for a 0.5-μJy detection threshold at 15 μm compared with state-of-the-art capabilities in the visible. The dashed line represents the radius detection threshold at $V_{mag} \approx 27$ (ref. 6). With a 0.5-μJy detection threshold (Extended Data Fig. 1), JWST can outperform searches in the visible up to 10 AU and by up to two orders of magnitude in size in the main belt.

valid between 100 m and approximately 10 m. The larger uncertainty associated with the steeper part of the SFD is because of the large uncertainties on the sizes (about 25%)—primarily driven up by the orbital-configuration uncertainty—that result in a wide range of steep SFDs matching the observed size distribution (Extended Data Fig. 6).

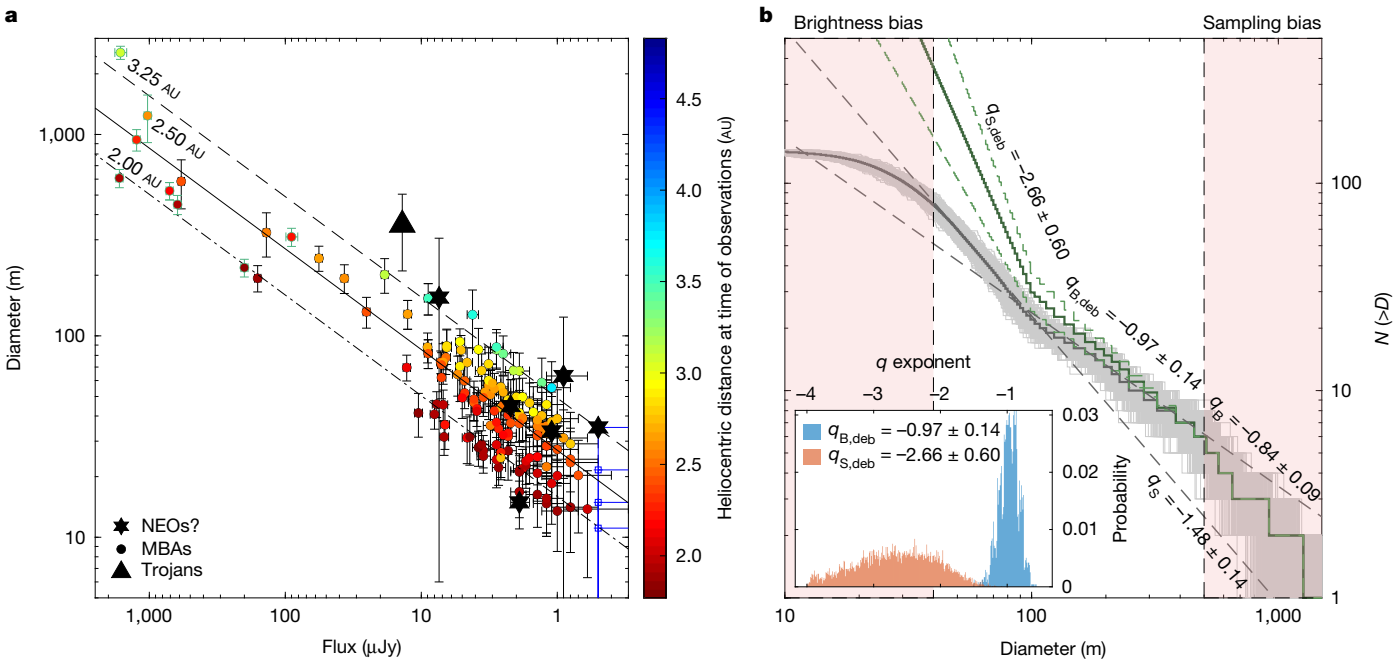

Fig. 3 | Flux–diameter and size–frequency relationships for the 146 asteroids detected with JWST/MIRI. a, Fluxes, diameters and heliocentric distances of the detected asteroids. The dashed-dotted, solid and dashed lines represent the size–flux relationships for objects at 2.00, 2.50 and 3.25 AU, respectively. Known asteroids (green) have smaller size uncertainties owing to known orbital configurations. Detections beyond the sensitivity threshold (approximately 0.5 μJy; Extended Data Fig. 3) are reported as upper limits on brightness and size using open blue symbols (bottom-right corner). **b**, Ensemble of cumulative SFDs built from 1,000 perturbed asteroid diameters to propagate the size uncertainties onto the SFD estimate (grey) using the Monte Carlo method[52] together with the debiased SFDs (green) (see Methods for details). Median raw and debiased SFDs are shown as solid lines. The debiased SFD presents two distinct regimes with exponents $q_{S,deb} = -2.66 \pm 0.60$ for small sizes and $q_{B,deb} = -0.97 \pm 0.14$ for big sizes (1σ interval between green dashed lines, probability distributions in inset)—$N(>D) = CD^q$, transition at roughly 100 m. The latter is consistent with ref. 34, reporting $q = -1.05 \pm 0.05$. Exponents before debiasing the SFDs for the size uncertainties are shown in the bottom-right corner.

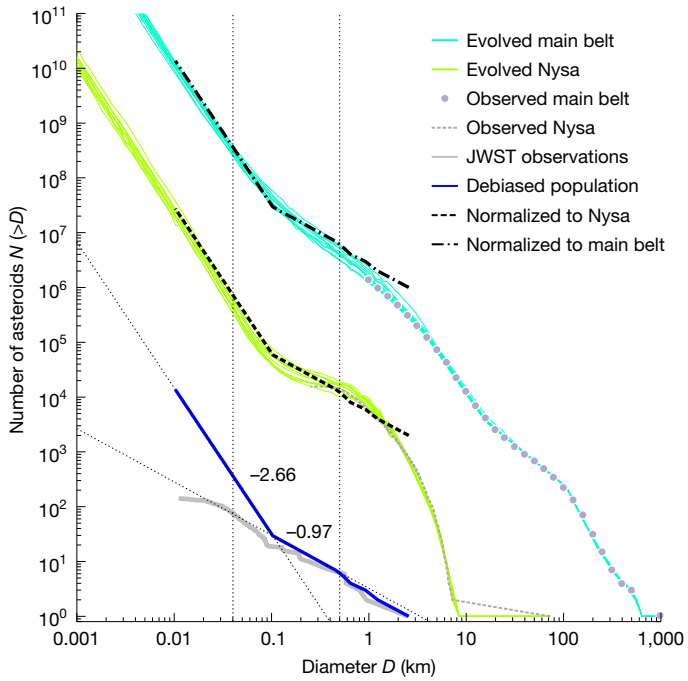

Fig. 4 | Asteroids observed by JWST have an SFD with a break at about 100 m, revealing a population in collisional equilibrium. The observed (grey) and debiased (blue) cumulative SFDs, $N(>D) = CD^q$, are shown together with corresponding slopes q (dotted lines). According to the collisional model from ref. 13, this corresponds exactly to the main-belt population between 1,000 m and approximately 50 m (aquamarine). Furthermore, evolved asteroid families show similar exponents owing to continuing collisions with the main-belt population. The Nysa family is plotted for comparison (lime), with a different normalization of the JWST data (dashed line).

This steeper slope is characteristic of the strength regime of fragmentation[29]. In fact, bodies approximately 100 m in size are among the weakest in the Solar System[30]. Their studies thus provide unique insights into realistic asteroidal materials.

At decametre sizes, small bodies are most probably fragments of bigger bodies, linked to recent disruptions and known asteroid families[13,19]. The associations of unknown asteroids are based on the same methodology; on orbits of known objects located close to the JWST FoV (Extended Data Fig. 7). More specifically, the Nysa family was sampled, together with the Polana, Massalia, Koronis2 and/or Karin families (Supplementary Table 1). In particular, the synthetic SFD of the Nysa and Polana families exhibit similar slopes that match the observations in both the shallow and steep regimes (Extended Data Fig. 8). According to the collisional model from ref. 31, their ages are on the order of 200 and 600 My, respectively. Consequently, sub-kilometre bodies should be in a collisional equilibrium. Other families exhibit a variety of slopes, especially because some of them are young[13]. At the decametres sizes, we expect the Massalia family to be dominant, as it is the source of the most common meteorites[14]. Nonetheless, when asteroids are sampled from several families, the resulting SFD is indeed a combination of steep and shallow slopes, resembling the distribution of the whole asteroid belt (Fig. 4).

Compared with previous pencil-beam surveys[32–35], our observations show on one hand a continuation of the shallow slope down to much smaller sizes than previously thought (Fig. 3b). For example, observations obtained by the Hubble Space Telescope[35] were only complete to $V \approx 23$ mag, corresponding to approximately 500 m, and reaching as far as $V \approx 28$ mag, similar to the deepest ground-based observations[6]. On the other hand, when debiasing the JWST observations, we find that the slope is steeper than previously thought, with a clear slope increase around 100 m. It is suggestive of the first and long-awaited evidence of a population that is evolving by collisions and at the same time moving from the main belt to the NEO space[12].

Because the transport itself is size-dependent owing to the Yarkovsky effect[36], the YORP effect[37] or thermal disruptions[38], the SFD of NEOs is substantially different from its source region. Observations of more than 30,000 NEOs[11,12] confirm a slope transition at about 100 m. As the slopes in the NEO region are already known ($q = 2.83 \pm 0.04$ and 1.64 ± 0.02; according to ref. 39), JWST observations offer the prospect of finally constraining transport mechanisms.

Prospects and planetary-defence efforts

Looking ahead, it is anticipated that JWST will be observing 15–20 exoplanet host stars for at least 500 h with MIRI[40]—a first step on the roadmap for the atmospheric characterization of (warm) terrestrial exoplanets[41], following a similar observing strategy to that followed to acquire the data used here[42,43]. As a large fraction of the host stars amenable for such studies are fortuitously found within 20° of the ecliptic, these 500 h will yield hundreds more decametre asteroids. Also, an average of about 1,800 h of MIRI observations were gathered per cycle in cycles 1 to 3. We thus expect that JWST will detect thousands of decametre asteroids per cycle. Such a substantial increase in sample size—especially if combined with a multivisit observation strategy to recover orbits precisely and multiband observations to constrain the thermal and rotation properties of the objects—will reduce substantially the uncertainties on the SFD slope, allowing to disentangle between different families and study the source regions of meteorites[13,14,31] 'in situ'.

Beyond the detection of asteroids that are otherwise undetectable, JWST can also yield infrared rotation curves of large (that is, ≳300 m) asteroids, thereby allowing their further characterization (Extended Data Fig. 4). The insights gained from JWST's infrared rotation curves of asteroids will be particularly valuable in two ways. First, their precision greatly exceeds their counterpart in the visible. Second, unlike visible rotation curves, they are mostly insensitive to surface topography, which results in reduced degeneracy with the albedo (similar to the size-estimation process in the infrared). As rotation rates can inform the origin and evolution of the asteroid family[44–46], their relationship to the break-up barrier[47] and even be used to derive their internal properties during close encounters[48], JWST is also poised to further our understanding of asteroid families and meteorite source bodies through rotation measurements.

There is thus a great deal of synergy between JWST and other facilities dedicated to the study of minor bodies, such as the Rubin observatory[49]—an all-sky survey in the visible aiming at discoveries of 100-m asteroids—and the Near-Earth Object Surveyor mission[50], with its unprecedented potential for the discovery and characterization of NEOs. Combining the expected discoveries of such dedicated facilities with the capabilities of JWST presented here will finally allow to constrain dynamical and collisional models all the way down to 10 m.

This synergy will extend beyond scientific endeavours and support planetary-defence efforts. Although planetary defence often seems to be associated with preventing events such as the impact that led to the extinction of the dinosaurs[51], decametre objects offer non-negligible threats that occur at much higher rates—rates are proportional to $D^{-2.7}$, leading to decametre impactors being roughly 10,000 times more frequent than kilometre-sized ones[2]. Decametre objects can lead to megaton explosions, leaving behind kilometre-sized craters. They are in fact at the origin of relatively recent events of importance on Earth, such as Chelyabinsk[10], Tunguska[3], Barringer[4] or Steinheim[5]. The capability of JWST to observe decametre objects all the way to the main belt (including NEOs at their aphelion) while deriving tighter (that is, nearly albedo-independent) sizes highlights its unique capability to monitor and study with great precision possible future impactors

detected closer to Earth by other surveys, thereby making JWST an important asset for future planetary-defence efforts.

Online content

Any methods, additional references, Nature Portfolio reporting summaries, source data, extended data, supplementary information, acknowledgements, peer review information; details of author contributions and competing interests; and statements of data and code availability are available at https://doi.org/10.1038/s41586-024-08480-z.

1. Cheng, A. F. et al. AIDA DART asteroid deflection test: planetary defense and science objectives. *Planet. Space Sci.* **157**, 104–115 (2018).
2. Brown, P., Spalding, R. E., ReVelle, D. O., Tagliaferri, E. & Worden, S. P. The flux of small near-Earth objects colliding with the Earth. *Nature* **420**, 294–296 (2002).
3. Chyba, C. F., Thomas, P. J. & Zahnle, K. J. The 1908 Tunguska explosion: atmospheric disruption of a stony asteroid. *Nature* **361**, 40–44 (1993).
4. Chao, E. C. T., Shoemaker, E. M. & Madsen, B. M. First natural occurrence of coesite. *Science* **132**, 220–222 (1960).
5. Stöffler, D., Artemieva, N. A. & Pierazzo, E. Modeling the Ries-Steinheim impact event and the formation of the moldavite strewn field. *Meteorit. Planet. Sci.* **37**, 1893–1907 (2002).
6. Reddy, V. et al. Near-Earth asteroid 2012 TC4 observing campaign: results from a global planetary defense exercise. *Icarus* **326**, 133–150 (2019).
7. Bottke, W. F. et al. The fossilized size distribution of the main asteroid belt. *Icarus* **175**, 111–140 (2005).
8. Farinella, P., Vokrouhlický, D. & Hartmann, W. K. Meteorite delivery via Yarkovsky orbital drift. *Icarus* **132**, 378–387 (1998).
9. Chesley, S. R. et al. Direct detection of the Yarkovsky effect by radar ranging to asteroid 6489 Golevka. *Science* **302**, 1739–1742 (2003).
10. Brown, P. G. et al. A 500-kiloton airburst over Chelyabinsk and an enhanced hazard from small impactors. *Nature* **503**, 238–241 (2013).
11. Harris, A. W. & Chodas, P. W. The population of near-earth asteroids revisited and updated. *Icarus* **365**, 114452 (2021).
12. Nesvorný, D. et al. NEOMOD 2: an updated model of Near-Earth Objects from a decade of Catalina Sky Survey observations. *Icarus* **411**, 115922 (2024).
13. Brož, M. et al. Young asteroid families as the primary source of meteorites. *Nature* **634**, 566–571 (2024).
14. Marsset, M. et al. The Massalia asteroid family as the origin of ordinary L chondrites. *Nature* **634**, 561–565 (2024).
15. Müller, T. G. et al. Asteroids seen by JWST-MIRI: radiometric size, distance, and orbit constraints. *Astron. Astrophys.* **670**, A53 (2023).
16. Tyson, J., Guhathakurta, P., Bernstein, G. & Hut, P. Limits on the surface density of faint Kuiper Belt objects. *Bull. Am. Astron. Soc.* **24**, 1127 (1992).
17. Shao, M. et al. Finding very small near-earth asteroids using synthetic tracking. *Astrophys. J.* **782**, 1 (2014).
18. Burdanov, A. Y., Hasler, S. N. & de Wit, J. GPU-based framework for detecting small Solar System bodies in targeted exoplanet surveys. *Mon. Not. R. Astron. Soc.* **521**, 4568–4578 (2023).
19. Nesvorný, D., Brož, M. & Carruba, V. in *Asteroids IV* (eds Michel, P. et al.) 297–321 (Univ. Arizona Press, 2015).
20. Gladman, B. & Kavelaars, J. J. Kuiper Belt searches from the Palomar 5-m telescope. *Astron. Astrophys.* **317**, L35–L38 (1997).
21. Bernstein, G. M. et al. The size distribution of trans-Neptunian bodies. *Astron. J.* **128**, 1364–1390 (2004).
22. Zhai, C. et al. Detection of a faint fast-moving near-Earth asteroid using the synthetic tracking technique. *Astrophys. J.* **792**, 60 (2014).
23. Heinze, A. N., Metchev, S. & Trollo, J. Digital tracking observations can discover asteroids 10 times fainter than conventional searches. *Astron. J.* **150**, 125 (2015).
24. Hasler, S. N. et al. Small body harvest with the Antarctic Search for Transiting Exoplanets (ASTEP) project. *Mon. Not. R. Astron. Soc.* **526**, 3601–3609 (2023).
25. Tedesco, E. F., Noah, P. V., Noah, M. & Price, S. D. The Supplemental IRAS Minor Planet Survey. *Astron. J.* **123**, 1056–1085 (2002).
26. Usui, F. et al. Asteroid catalog using Akari: AKARI/IRC mid-infrared asteroid survey. *Publ. Astron. Soc. Jpn* **63**, 1117–1138 (2011).
27. Mainzer, A. et al. Preliminary results from NEOWISE: an enhancement to the Wide-field Infrared Survey Explorer for Solar System science. *Astrophys. J.* **731**, 53 (2011).
28. Rieke, G. H. et al. The mid-infrared instrument for the James Webb Space Telescope, VII: the MIRI detectors. *Publ. Astron. Soc. Pac.* **127**, 665 (2015).
29. Dohnanyi, J. S. Collisional model of asteroids and their debris. *J. Geophys. Res.* **74**, 2531–2554 (1969).
30. Benz, W. & Asphaug, E. Catastrophic disruptions revisited. *Icarus* **142**, 5–20 (1999).
31. Brož, M. et al. Source regions of carbonaceous meteorites and near-Earth objects. *Astron. Astrophys.* **689**, A183 (2024).
32. Gladman, B. J. et al. On the asteroid belt's orbital and size distribution. *Icarus* **202**, 104–118 (2009).
33. Ryan, E. L. et al. The kilometer-sized Main Belt asteroid population revealed by Spitzer. *Astron. Astrophys.* **578**, A42 (2015).
34. Maeda, N. et al. Size distributions of bluish and reddish small main-belt asteroids obtained by Subaru/Hyper Suprime-Cam. *Astron. J.* **162**, 280 (2021).
35. García-Martín, P. et al. Hubble Asteroid Hunter. III. Physical properties of newly found asteroids. *Astron. Astrophys.* **683**, A122 (2024).
36. Vokrouhlický, D. A complete linear model for the Yarkovsky thermal force on spherical asteroid fragments. *Astron. Astrophys.* **344**, 362–366 (1999).
37. Rubincam, D. P. Radiative spin-up and spin-down of small asteroids. *Icarus* **148**, 2–11 (2000).
38. Granvik, M. et al. Super-catastrophic disruption of asteroids at small perihelion distances. *Nature* **530**, 303–306 (2016).
39. Nesvorný, D. et al. NEOMOD: a new orbital distribution model for near-Earth objects. *Astron. J.* **166**, 55 (2023).
40. Redfield, S. et al. Report of the Working Group on Strategic Exoplanet Initiatives with HST and JWST. Preprint at https://arxiv.org/abs/2404.02932 (2024).
41. TRAPPIST-1 JWST Community Initiative A roadmap for the atmospheric characterization of terrestrial exoplanets with JWST. *Nat. Astron.* **8**, 810–818 (2024).
42. Greene, T. P. et al. Thermal emission from the Earth-sized exoplanet TRAPPIST-1 b using JWST. *Nature* **618**, 39–42 (2023).
43. Zieba, S. et al. No thick carbon dioxide atmosphere on the rocky exoplanet TRAPPIST-1 c. *Nature* **620**, 746–749 (2023).
44. Farinella, P., Davis, D. R., Paolicchi, P., Cellino, A. & Zappala, V. Asteroid collisional evolution—an integrated model for the evolution of asteroid rotation rates. *Astron. Astrophys.* **253**, 604–614 (1992).
45. Bottke, W. F. Jr, William, F., Vokrouhlický, D., Rubincam, D. P. & Nesvorný, D. The Yarkovsky and YORP effects: implications for asteroid dynamics. *Annu. Rev. Earth Planet. Sci.* **34**, 157–191 (2006).
46. Carruba, V. et al. The population of rotational fission clusters inside asteroid collisional families. *Nat. Astron.* **4**, 83–88 (2020).
47. Polishook, D. Spin axes and shape models of asteroid pairs: fingerprints of YORP and a path to the density of rubble piles. *Icarus* **241**, 79–96 (2014).
48. Dinsmore, J. T. & de Wit, J. Constraining the interiors of asteroids through close encounters. *Mon. Not. R. Astron. Soc.* **520**, 3459–3475 (2023).
49. LSST Science Collaboration et al. LSST Science Book, Version 2.0. Preprint at https://arxiv.org/abs/0912.0201 (2009).
50. Mainzer, A. K. et al. The Near-Earth Object Surveyor mission. *Planet. Sci. J.* **4**, 224 (2023).
51. Alvarez, L. W., Alvarez, W., Asaro, F. & Michel, H. V. Extraterrestrial cause for the Cretaceous-Tertiary extinction. *Science* **208**, 1095–1108 (1980).
52. Metropolis, N. & Ulam, S. The Monte Carlo method. *J. Am. Stat. Assoc.* **44**, 335–341 (1949).

Methods

JWST image processing

Data from PIDs 1177 and 2304 were acquired with JWST/MIRI in October and November 2022 using FULL subarray mode, resulting in 112″ × 113″ (1,024 × 1,032 pixels^2) FoV. Data from PID 3077 were obtained in November 2023 in BRIGHTSKY subarray mode, resulting in a smaller FoV of 56.3″ × 56.3″ (512 × 512 pixels^2). All programmes used the F1500W filter and FASTR1 readout mode.

For our asteroid search, we downloaded exposure raw data products (*uncal.fits files) from the Barbara A. Mikulski Archive for Space Telescopes. Then we ran stages 1 and 2 JWST Science Calibration Pipeline version 1.13.4 to produce calibrated *calints.fits files. These files are single exposures containing results for all integrations in an exposure with world coordinates and photometric information. Every *calints.fits 3D data file was sliced into a set of 2D data files containing the pixel values for each integration with exposure time of 38.9 s for PIDs 1177 and 3077 and 36.1 s for PID 2304. For PIDs 1177 and 2304, we trimmed 2D data files to exclude parts of the detector designed for coronagraphic imaging, resulting in a useful FoV of 72″ × 113″ (654 × 1,032 pixels^2). Each 2D data file was then corrected for sky background using the Photutils[53] Python software package. Background-subtracted images were then searched for any moving objects that happen to cross the FoV.

Detection of asteroids using synthetic tracking and their flux estimation

We used our custom-build wrapper[18,24] around the Tycho Tracker[54] synthetic tracking software to explore a wide range of motion vectors and generating trial exposure stacks for each vector. No restrictions on position angle were used and speed was in the range 0.001–1.200 arcsec min^{-1}. Our speed limits were set to enable detection of objects moving as slow as 0.5 pixels per hour and fast-moving objects streaking up to 10 pixels in a single integration. Each trial exposure stack was computed by shifting the exposures according to the motion offsets associated with the current vector. If an object had motion similar to that of the given vector, it was extracted from the trial exposure stack by the detection process. We grouped images to detect faster-moving objects by dividing the image sequence from one JWST visit into overlapping groups of 100 exposures, ensuring the detection of an asteroid if it appears in at least 50% of the group's images. After detecting fast-moving objects, we performed a search for slower-moving objects by searching all of the images from one JWST visit (up to 350 exposures for PIDs 1177 and 2304 and up to 1,000 exposures for PID 3077). A set of candidate detections (tracks) was returned with corresponding speed, position angle, pixel coordinates and SNR of detection.

We cross-matched every track with already known objects using the NASA Jet Propulsion Laboratory (JPL) Small-Body Identification API (https://ssd-api.jpl.nasa.gov/doc/sb_ident.html). A match was made if a known object was positioned within 0.1′. We were able to detect 8 known asteroids and 138 unknown asteroids with SNR ≥ 5 (Extended Data Table 1 and Supplementary Table 1).

We measured the flux of each asteroid using aperture photometry, using a circular aperture with a radius of 2.5 × full-width at half-maximum (FWHM) of the asteroids' point spread function (PSF) in the shifted and stacked image. The sky background was measured in an annulus beyond the asteroid aperture using a median sky-fitting algorithm. The annulus had a radius of 4 × FWHM and a width of 2 × FWHM. We applied similar aperture photometry to estimate the flux of the TRAPPIST-1 star (the only stellar object in the FoV) and calculated the flux ratio of each asteroid to TRAPPIST-1. Previous studies[42] have shown that the absolute flux of TRAPPIST-1 in the F1500W band is stable at 2,590 ± 80 μJy. We determined the absolute flux values of the asteroids using this reference flux of TRAPPIST-1. Flux estimates and their associated errors can be found in Extended Data Table 1 and Supplementary Table 1.

For the 15 asteroids crossing the PSF of TRAPPIST-1 or detector artefacts, we derived their fluxes based on several stacks of integrations that do not include crossing. We note that the same procedure of using several stacks of integrations was used to check for flux consistency for all objects.

We do not perform colour correction here as it is mostly constant between asteroids and thus does not affect the derived SFD (our core finding). Colour corrections for the MIRI bands were discussed in ref. 15 and are needed because the spectral energy distribution of the reference (typically a calibration star, here TRAPPIST-1) is substantially different from the asteroids across the MIRI bandpass. For typical NEO and MBA temperatures between 200 and 400 K, these corrections are only 1% in the F1500W band. Only for very distant objects (effective temperatures of 100 K or below) would the required colour correction reach the 5% level. We thus omitted this correction, as the final diameter errors are dominated by the orbital uncertainties. Future studies targeting individual asteroid detection (rather than performing population studies, as done at present) will require such colour corrections.

Asteroid detection efficiency

We conducted a series of injection-recovery tests to evaluate our asteroid-detection efficiency. We injected a 4 × 11 grid of synthetic moving objects, each with various flux values (see below), into 100 72″ × 113″ (654 × 1,032 pixels^2) FITS files from PID 1177. Synthetic objects were placed in such a way that they spend all the time (approximately 1 h) in the FoV, had random position angles from a uniform distribution between 70 and 80° and random speeds sampled from an actual speed distribution of the detected objects (0.02–1.10 arcsec min^{-1}). Before running the synthetic tracker, we subtracted the sky background. After completion of the synthetic tracking, we compared the detected objects with the injected ones. We repeated this test four more times for the same flux value as a sensitivity analysis for our estimated recovery rate as a function of flux. In total, we performed 11 sets of injection-recovery tests with objects having flux values of 3.50, 3.00, 2.50, 2.00, 1.50, 1.25, 1.00, 0.75, 0.50, 0.25 and 0.1 μJy. Our recovery rate is ≥80% for objects down to 1.5 μJy (Extended Data Fig. 1), which then decreases to 50 ± 2% at 1.1 μJy. The derived cutoff is 1.1 μJy, with an observation bias starting at about 1.5 μJy (39 out of 138 unknown objects have fluxes smaller than 1.5 μJy). This translates to an observational bias emerging in the 20–40-m-diameter regime with a sharp cutoff by about 10 m.

For false positives, as seen in other asteroid search surveys, spurious associations of noise can coadd and lead to apparent signals that may be identified as possible detection[55,56]. Such noise patterns, however, typically manifest as a handful of bright pixels on the shifted and stacked image. By contrast, our confirmed detections exhibit tens of bright pixels arranged in a symmetric PSF, which is clearly distinguishable from the background (Fig. 1b and Supplementary Fig. 1). To confirm that aspect, we selected a series of data cubes in which we detected objects and performed numerous random perturbations of the image timestamps to assess whether spurious associations of noise could lead to convincing false positives. Out of these dozens of random perturbations for five different observing epochs, none of the best detection candidates presented more than a handful of bright pixels arranged symmetrically and thus look like the 138 detections shown in Supplementary Fig. 1. Also, most of these spurious detections do not appear in both the first and second halves of the shifted and stacked images, a clear flag for a spurious signal.

Orbit estimations

To estimate the sizes of the unknown asteroids from their infrared fluxes, we require their positions at the time of observations with respect to the Sun and JWST (observer), that is, observer–target (O–T) distance, Sun–target (S–T) distance and the corresponding S–T–O phase angle. Owing to the short duration of the asteroids' arcs in our

data, a large ensemble of possible orbital configurations exist for each object—even in the case of the longest observing arc of 8 h of unknown asteroid #91. To overcome this bottleneck, we developed a method using ensembles of orbital configurations of known objects that are present around JWST FoV as proxies (or priors) to derive posterior probability distributions of O–T and S–T distances and S–T–O phase angles for unknown asteroid distances. We assume that unknown asteroids must be related to faint known asteroids, because the former are fragments of bigger bodies (either released just after a break-up or created by collisional cascade), that is, they are genetically linked[13,14].

For every JWST visit, we obtained a list of all known asteroids predicted to be within a 6×2 degree^2 (RA × dec.) reference field around the TRAPPIST-1 star using the JPL Small-Body Identification API. We queried JPL Horizons API (https://ssd-api.jpl.nasa.gov/doc/horizons.html) for the speed, position angle, O–T distance, S–T distance and the corresponding S–T–O phase angles for each known asteroid. Then, every unknown asteroid was placed in the speed/position angle parameter space and known objects in their proximity were used as proxies/priors to constrain their orbital configuration (Extended Data Fig. 2).

We first used a series of ellipses to select proxies within a certain distance of each unknown object and test the sensitivity of the inferred properties. The proxy1s ellipse is defined as an ellipse with width of 5% of the unknown object's speed and an absolute value 0.5° for position angle (which correspond respectively to the typical 1σ uncertainties on measured speed and position angle by our pipeline). The proxy3s and proxy10s ellipses are 3 × proxy1s's and 10 × proxy1s's ellipses, respectively. We assigned a distance to a particular unknown asteroid as a mean value of O–T distances to each proxy, that is, known asteroids in different ellipses. We carried out similar calculations to the S–T distances and the corresponding S–T–O phase angles.

We assessed the sensitivity of our distance estimates to different sizes of the reference field around the TRAPPIST-1 star, which confirmed negligible dependencies when compared with the derived uncertainties (that is, spread in O–T distance, S–T distance and S–T–O angle). As a proof of concept, we tested this method on eight known asteroids observed at different epochs. We removed their true speed and position angle values from the speed/position angle parameter space and treated them as unknown objects. We found that, in all instances, the proxy3s and proxy10s ellipses provide enough proxies to yield estimates within 1σ of the true values—1σ error bars are typically between 0.2 and 0.3 AU. Extended Data Fig. 3 shows an application of the method to the eight known asteroids. All of the known and derived properties of the eight 'validation objects' are reported in Extended Data Table 1.

Although we observed that the proxy3s and proxy10s ellipses provide enough proxies to yield reliable estimates, we also observe that, for a handful of known asteroids, the proxy10s ellipses lead to substantially larger uncertainties owing to a large number of proxies associated with different families joining the sample. Also, we noticed that the approach aiming at using fixed ellipses in the speed/position angle parameter space can lead to a large amount of discrepancies between the number of proxies returned for each object. In a final application of this proxy-based approach, we search for a convergence of both the estimated distances and the uncertainties on these distances by using the N closest proxies. We find that, for all but asteroids #66 and #106, the values converge and are stable when $10 \leq N \leq 25$ (example in Extended Data Fig. 2c). Below about ten proxies, small-number statistics lead to biases on the estimated orbital configuration and related uncertainty. Above about 25 proxies, we often start sampling other populations, leading to artificially larger uncertainties (and often a small bias on the orbit estimation, drifting with increasing N). For asteroids #66 and #106, these are flagged as possible NEOs (Extended Data Table 2), which have very few close proxies and have, among the closest 25 proxies, one or more outliers, which we remove manually to avoid biases. We present the example of asteroid #66 in Extended Data Fig. 2d). Unknown asteroid #66 is probably a NEO observed close to aphelion and has a limited number of close proxies. As a result, its 19th and 20th closest proxies are clear outliers (specifically trans-Neptunian objects, 2000 OJ67 and 2000 PN30), leading to a sudden jump of its derived uncertainty (blue curve). For all other asteroids, we use the 17 closest proxies under the label 'proxy17n'.

To complete our validation, we turned to a larger sample of known objects, randomly selecting a total of approximately 20,000 known asteroids in the reference field across all epochs and assessing their distance through proxy17n. Doing so, we find that the median deviation between true distance and estimated distance is 0.007 AU with a standard deviation of 0.24 AU. Considering the uncertainties associated with each individual proxy17n estimation (typically between 0.2 and 0.3 AU, as mentioned above), this shows an excellent match between the spread at the population level and the uncertainty at the level of individual estimates. We find that only 0.85% of the 20,000 asteroids have an estimated distance more than 3σ away from truth, which is consistent with the distribution and small-number statistics considering our main sample size (138). Also, all of these outliers seem to be automatically flagged as outliers, as their proxy17n distance estimates return large individual uncertainties (tapping into different populations).

Assessing the probable association of the unknown objects

For each of the 138 unknown objects, we estimated their probable associations to individual populations. We used the same lists of known asteroids (proxies) close to the FoV and plotted their proper orbital elements (semimajor axis a_p, eccentricity e_p, inclination i_p). If most of the proxies for an object were located close to a known sizeable family[19], we assessed this association as probable. We also verified the respective speed and position angle of unknown asteroids. If they were too low, too high or too offset with respect to typical values of MBAs, the associations were the NEOs, Hildas or trojans. If the number of known objects was too limited or they were too scattered, we do not report any association. Our results are summarized in Extended Data Table 2.

On the expected population of NEOs crossing the FoV

To assess the sensitivity of this pencil-beam survey to the NEO population, we derived the fraction of NEOs in the 6×2 degree^2 reference field introduced in the previous section. We found that only 1.1% of all known objects predicted to be within the reference field at each observing epoch are NEOs. Given that we detect about 130 MBAs, this means that roughly 1.5 NEOs could be expected.

We used the derived position angle and speed to assess for the probable association of each detection and found that up to six objects could be NEOs (Extended Data Table 2). This difference is a natural consequence of the facts that: (1) JWST/MIRI observations were carried out in the mid-infrared, making them sensitive to much smaller sizes (sub-kilometre versus decametre), as NEOs are hotter, and (2) the SFD of NEOs is steeper than the SFD of the MBAs owing to the size-dependent transport. We thus consider our results to be consistent.

Debiasing the absolute magnitudes of asteroids

The size calculation of known asteroids relies on refined and debiased absolute H magnitude estimates of asteroids, which were derived through a new correction method, DePhOCUS[57]. The method performs debiasing of astro-photometric observations from the Minor Planet Center (MPC) with corrections using a statistical analysis based on an accurate reference of 468 asteroids with more than 450,000 observations in total. The method allows a derivation of 17 revised notable colour bands, 90 catalogue and 701 observatory corrections (significance level $P = 0.90$), which lead to a reduction of more than 50% in the root mean square (r.m.s.) of the asteroids' phase curve and a more accurate estimation of the parameters of the H–G phase curve model, in which G is the slope parameter. We used the corrections to debias the observations at the MPC for all known asteroids in the present study

and compute the absolute H magnitude values and their uncertainties, assuming G = 0.15.

Size and albedo determination

We performed radiometric analysis of all detected asteroids using the Near-Earth Asteroid Thermal Model (NEATM[58]). The NEATM was originally developed for near-Earth asteroids but is now also widely applied to asteroids in the main belt and beyond (see, for example, refs. 59–61). In this model, the asteroids are approximated by non-rotating and smooth spheres that are in instantaneous thermal equilibrium with the incident solar radiation. This allows to calculate the temperature of each surface element through $\mu \times (1 - A) \times S_{sun}/r^2 = \epsilon\eta\sigma T^4$, in which μ is the cosine of the angle between the element's normal and the direction towards the Sun, A the bolometric Bond albedo, S_{sun} the solar incident energy at 1 AU, r the heliocentric distance, ϵ the emissivity (a fixed value of $\epsilon = 0.9$ is taken) and σ the Stefan–Boltzmann constant. The infrared beaming parameter η was introduced as a free parameter. It can be determined from a fit to multiband infrared measurements (as originally done in ref. 58) or calculated from published linear phase-angle relations (for example, refs. 59,61,62). For specific asteroid groups, average η values are often taken, for example, $\eta = 1.4$ for near-Earth asteroids[63], $\eta = 1.2$ for Mars-crossing asteroids[60], $\eta = 1.0$ for MBAs[59], $\eta = 0.77$ for Hildas and Jupiter trojans[64] or $\eta = 1.2$ for trans-Neptunian objects[65]. Reference 59 also gave η distributions for inner, middle and outer main-belt objects, with peak values at around 0.95–1.10 for inner, 0.9–1.0 for middle and 0.85–0.95 for outer MBAs. For the interpretation of our single-band data, it is not possible to determine object-specific η values from the measurements. Therefore, we took the η relation in ref. 61: $\eta(\alpha) = 0.76(\pm0.03) + (0.009 \pm 0.001)\ \mathrm{deg}^{-1}$. This relation is based on the analysis of more than 5,000 asteroids, all observed in two broad bands at 9 and 18 μm. As both bands are close to the MIRI F1500W band, we consider this solution as the most appropriate for our analysis. However, instead of the given parameter error, we use a more conservative η error of ±10% for the NEATM size and albedo calculations.

For very small asteroids (on the decametre scale), the NEATM model is not well tested. Also, small objects tend to spin faster[66]. In this case, their surface temperature would be better described by the isothermal latitude model (ILM) or fast-rotating model (FRM)[67] (see also discussions in ref. 68). We tested the impact of these model assumptions for the size calculation of typical MBAs. The smallest-size objects are only detected at small heliocentric distances <2.5 AU and seen under phase angles between 20° and 30°. Assuming that such fast-rotating asteroids are nearly isothermal (modelled by a beaming parameter of 3.14 and lacking flux changes with phase angle), we find that the FRM-derived sizes are about 1.5–1.6 times larger than the default NEATM-derived sizes. However, the size and rotation-rate limits for the NEATM-to-FRM transition are not known. Reference 69 found beaming parameters of 1.0–1.5 (very similar to our NEATM calculations) for about 50 NEOs with sizes between about 8 m and about 100 m. Reference 70 looked at the Yarkovsky semimajor axis drift rate of a rapidly rotating asteroid. They found an unexpectedly low thermal inertia, indicative of a highly porous or cracked surface. Both studies show no indications that fast-rotating decametre objects are predominantly isothermal and thus support the use of the NEATM over the FRM.

Although we recommend that future observations aim for immediate follow-up of detections (within a few days) to place tight constraints on the orbit and are performed in a different MIRI band to inform the thermal and rotation properties of the detections, we note that the core result of our findings (namely, a steep SFD downward of about 100 m) is independent from using the NEATM or the FRM. Indeed, using one or the other below a certain size primarily results in multiplying all sizes by a factor of roughly 1.5, thereby keeping the SFD slope constant. Also, that possible transition is expected at small sizes below our cutoff at about 40 m for the slope estimate.

Properties of the eight known asteroids

The errors in H magnitude, η and the measured flux are all considered in the NEATM calculations. An absolute flux error of 6% (10%) leads approximately to uncertainty of 3% (5%) for the size and 5% (9%) for the albedo, whereas the 10% higher (lower) η value increases (decreases) the size. For these known asteroids, the dominating sources of uncertainty for the size estimates are the assumptions for η and the absolute uncertainty for the fluxes, whereas for the albedo, the large uncertainty in H magnitude drives the final errors. Extended Data Table 1 summarizes the NEATM input values and our findings for the eight known asteroids among the serendipitous detections.

Among all known asteroids, (194793) 2001 YP90 was observed by JWST continuously for the longest period of time (3 h) and the data show substantial flux variations, indicating an elongated body (Extended Data Fig. 4) with a minimum (maximum) flux of 550 μJy (1,300 μJy). These flux values translate into diameters of 640 ± 43 m (922 ± 70 m) and albedo values of $0.51^{+0.17}_{-0.14}$ ($0.24^{+0.10}_{-0.07}$). Calculated diameters at minimum and maximum flux are first-order estimates for the elongation of the asteroid. Diameters and albedos reported in Extended Data Table 1 were calculated using an average flux of 1.03 μJy. The obtained JWST light curve is in good agreement with the data from ground-based telescopes (see the section 'Follow-up observations of the eight known asteroids').

Albedo values of asteroid 152630 (1997 GP4) derived from our radiometric analysis ($p_V = 0.29^{+0.12}_{-0.08}$) are in agreement with the expected value for S-type asteroids (0.26 ± 0.09 (ref. 71); see the section 'Follow-up observations of the eight known asteroids').

Out of the eight known MBAs, only (472944) 2015 GH28 has a published radiometric diameter. Reference 59 used 11 W3-band measurements from the WISE/NEOWISE spacecraft (from 15/16 February 2010, at $r_{helio} = 2.45$ AU, $\Delta = 2.23$ AU, $\alpha = 23.8°$, W3 band centre at 12 μm) to derive a size of 2,290 ± 390 m; no albedo was determined. This is in good agreement with our findings.

Properties of the objects with unknown orbits

For newly detected objects, we used the previously introduced population-driven constraints on their orbits (see the section 'Orbit estimations') to transform the measured F1500W fluxes into size estimates. As neither H magnitude nor albedo are known, we simply determined a default NEATM size and took the unknown properties into account when we estimate the size error. The procedure is described by the following steps:

1. We use the calculated O–T distance, S–T distance and the corresponding S–T–O phase angles from the 17 closest proxies (proxy17n) for each object.
2. For each of the proxy17n geometries, we translated the measured flux into a radiometric size through the NEATM. The NEATM calculations are performed for a geometric V-band albedo $p_V = 0.15$ and a beaming parameter η, which is calculated for the specific S–T–O phase angle (see the section 'Size and albedo determination'). The corresponding 17 sizes (per unknown object) are averaged.
3. The size error calculation take the following parameters into account: (1) standard deviation of the 17 proxy sizes (a typical 10% uncertainty on O–T translates into a 10% size uncertainty; the same is true for S–T); (2) absolute flux error (with a 10% flux error translating into a 5% size error); (3) further 5% size error originating from the 10% accepted variation in the beaming parameter; (4) size error introduced by the unknown albedo: a $p_V = 0.05$ (0.30) object (in comparison with $p_V = 0.15$) would give an approximately 2% larger (about 3% smaller) size. The first three error contributions have a nearly Gaussian distribution and are added quadratically. The albedo component is added at the end in a linear way, as we do not consider it an independent variable but rather account here uniformly for its whole range of possible values.

It is important to note that the derived size range for each object is dominated by the range of possible geometries and, for the low SNR detections, also by the absolute flux error. The different assumptions for the albedos and the beaming parameter are almost negligible in the radiometric size determination. All of the properties of the 138 new detections are reported in Supplementary Table 1.

For a validation of the method, we handled the eight known asteroids in exactly the same ways as the 138 unknown ones. The resulting solutions are shown in Extended Data Fig. 3 (based on S–T, O–T and S–T–O values derived from the orbital properties of proxy17n). The derived size ranges are very similar and agree within the error bars very well with the solutions given in Extended Data Table 1, for which their true orbits were used. The asteroids are reported in the same order as in Extended Data Fig. 3 and in Extended Data Table 1, that is, asteroid #1 is 2011 SG255 and asteroid #8 is (472944) 2015 GH28.

Follow-up observations of the eight known asteroids

We conducted ground-based follow-up observations of a set of known asteroids in our sample to better characterize their phase curve, colours and rotation period and amplitude. Observations of (194793) 2001 YP90 and 2021 FR9 were acquired with the 1-m Artemis telescope[72] of the SPECULOOS network[73] and with the 0.6-m TRAPPIST-North[74] telescope. 2021 FR9 was observed between 2 and 10 February 2024 at solar phase angles ranging from 1.8° to 4.3°. The photometry and magnitude calibration to the Johnson V band was performed using the Photometry Pipeline[75]. 2001 YP90 was observed between 1 February and 9 March 2024 at solar phase angles ranging from 2.9° to 20.9° and included longer observation runs to determine its rotation period. We determined a period of 5.7701 ± 0.0001 h and a relatively large amplitude of 0.87 ± 0.10 mag, indicating an elongated body (Extended Data Fig. 4).

A series of exposures with SDSS griz filters were also obtained for the asteroids 2001 YP90 and 1997 GP4 on 16 February with the 4.3-m Lowell Discovery Telescope (previously known as Lowell's Discovery Channel Telescope)[76]. These spectro-photometric observations allowed to determine the taxonomic types for these two bright asteroids. For 2001 YP90, the taxonomic fits r.m.s. values suggest that a K type is the only good fit to the data. Derived values of albedo from our radiometric analysis (see the section 'Properties of the eight known asteroids') are also compatible with K-type asteroids. For 1997 GP4, Sr type is the best fit but S or Sq types are close in terms of r.m.s. (Extended Data Fig. 5).

On the information content and sensitivity of the SFD

Before interpreting the SFD, we assessed its sensitivity to uncertainties and biases to determine the size regime over which its information content can reliably be translated into scientific inferences. First, we developed a framework to adequately propagate the large uncertainties (Fig. 3a) on the asteroid sizes onto the SFD. To do this, we followed the Monte Carlo method[52] and generated an ensemble of 10,000 randomly perturbed diameters for each asteroid (Fig. 3b, grey curves). As discussed in the previous section, the size uncertainties are primarily driven by the uncertainty on the orbital configuration (O–T and S–T each contribute roughly 10–15%), in comparison with the contributions from the flux, beaming parameter and albedo uncertainties respectively contributing to a size uncertainty of about 3–10%, about 5% and about 2–4%. The probability distributions of the main variables/contributors (O–T, S–T and flux) are found to follow Gaussian distributions. The probability distribution for the beaming parameter only marginally deviates from a Gaussian for the present application, whereas the albedo is best approximated by a uniform distribution between 0.05 and 0.30. The size uncertainty thus primarily follows a uniform distribution with an average relative standard deviation of $\sigma_D/D \approx 25\%$, in which σ_D is the size uncertainty.

We note that, owing to the transformation from linear (sizes) to log (SFD) space, the uncertainty distribution on the SFD is asymmetrical. This means that the SFD derived from the median sizes does not correspond to the actual median SFD. Therefore, not accounting for the size uncertainties when deriving the SFD estimates can lead to biases when the size uncertainties are important (especially in the regime driven by large Gaussian uncertainties owing to the wings of their distribution). In the present case, not accounting for the size uncertainty leads to an SFD estimate biased towards larger slope.

Similarly we note that it is pivotal to account for the expected distribution of uncertainties as well as the sample size when building the models to be compared with the SFD. Indeed, standard theoretical models are built assuming that a large number of asteroids are observed with a great precision on their sizes, which is not true in practice. To highlight that aspect, we offer the following simple case: a theoretical population in which all objects have the exact same size leading to a vertical SFD. Yet, any observation of this population will always return a spread of values owing to uncertainties on each individual size measurements, which will result in a sloped SFD. That apparent slope will be dependent on the uncertainty of the size estimates and the number of objects detected. Extended Data Fig. 6a further develops this point by comparing the true slope of an SFD to its apparent slope as a function of the measurement uncertainty considering here uncertainty distributed primarily in a Gaussian fashion. It shows that, for a regime in which $\sigma_D/D \gtrsim 5\%$, the apparent slope is systematically shallower. For the present study, it shows that the slopes of $q_S \approx -1.5$ and $q_B \approx -0.85$ respectively found for small and big sizes (transition at about 100 m, match with true (that is, debiased) slopes of $q_{S,deb} \approx -2.66$ and $q_{B,deb} \approx -0.97$). We use this slope mapping to debias our SFD and match with theoretical models (Fig. 4).

We note that, for the size-uncertainty regime of this study, a wide range of true slopes match with the observed $q_S = -1.47 \pm 0.13$ (Extended Fig. 6a). This results in a posterior probability distribution on $q_{S,deb}$ that is substantially wider than $q_{B,deb}$ (respective spread: 0.60 versus 0.14; Extended Data Fig. 6b). Future studies increasing the number of detections and/or the orbital constraints (for example, with a multi-visit follow-up strategy) will help reduce the uncertainties on the SFD, thereby allowing to disentangle between different families and study the source regions of meteorites[13,14,31] 'in situ'.

We then investigated observational biases (or sensitivity limits). The first bias of observational origin relates to our detection threshold at about 0.5 μJy. This threshold corresponds to a decrease in recovery rate that emerges around 1.5 μJy and translates into an observational bias emerging in the 20–40-m-diameter regime with a sharp cutoff by about 10 m (Fig. 3a and Extended Data Fig. 1), meaning that the current SFD cannot be readily used beyond 40 m. At the other end of the size regime, large asteroids crossing the FoV are rare owing to their lower occurrence rates. Therefore, the SFD derived from their detection is affected by small-number statistics. To assess the size threshold above which this occurs, we generated synthetic populations of one million objects with exponents ranging from $q = -2.0$ to $q = -0.7$ – $N(>D) = CD^q$ – and drew 10,000 random batches of 150 asteroids to assess the size regime over which the derived SFDs present an adequately small variance given our number of detections.

We find that the size cutoff for the sampling bias is dependent on the exponent, with a size cutoff ranging from 70 m for $q = -2.0$ to 1,200 m for $q = -0.7$ (Extended Data Fig. 6c,d). Through a series of draws (for example, Extended Data Fig. 6c) and for different q exponents, we find that the best marker for identifying the size cutoff (that is, when the slope starts diverging from the true slope) is $N \leq 7$. In other words, small-number statistics is the best marker for this sampling bias at large sizes.

This finding also shed lights on the substantial tension between the SFD estimate in the 40–100-m range and the number of 'large' asteroids found ($N(>300\text{ m}) = 9$). Indeed, the likelihood of a sample of 150 asteroids with a $q = -1.45$ to also present $N(>300\text{ m}) = 9$ is roughly 1:10,000 (that is, $\gtrsim 4\sigma$). This provides further support to the fitting of the SFD with a shallower slope beyond about 100 m, at which a transition is seen.

Interpretation of the SFD

Knowing which population has been sampled by our JWST observations is key for an interpretation. According to Extended Data Fig. 7, orbits of known faint objects located close to the JWST FoV are not evenly distributed across the main belt. Instead, they are associated to selected asteroid families, namely, to Polana, Nysa, Massalia, Koronis2 or Karin, which are both populous and preferentially close to the ecliptic plane, similar to the TRAPPIST-1 star. See Supplementary Table 1 for details.

The observed SFDs of individual families are substantially different (for example, Extended Data Fig. 8). Some of them are steep down to the observational limit, which occurs at about 1,000 m, depending on the respective heliocentric distance and albedo. Others exhibit a distinct break at around 5,000 m, below which the slope becomes shallower, with the exponent approximately −1.5, characteristic of a collisional equilibrium at kilometre sizes. This is most probably the result of long-term collisional evolution of families[13,14]. In other words, young families (Massalia, Koronis2 and Karin) have a steep SFD, whereas old families (Polana, Nysa and so on) have a shallow SFD at sub-kilometre and decametre sizes.

Data availability

The data used here are publicly available on the Mikulski Archive for Space Telescopes (MAST) at the Space Telescope Science Institute (STScI) and are associated with programmes 1177, 2304 and 3077, with T.P.G., L.K. and M.G. as principal investigators, respectively. The processed JWST images used to create Fig. 1 are available under the 'JWST TRAPPIST-1' dataset on the Tycho Tracker website at https://www.tycho-tracker.com/download. Astrometric measurements of unknown asteroids are available in a MPC isolated tracklet file (https://sbnmpc.astro.umd.edu/MPC_database/statusDB.shtml): tracklets AST001–AST139, submission_ids 2024-08-06T23:54:21.000_0000GBYm, 2024-08-07T20:19:18.001_0000GBhr, 2024-08-07T22:38:47.000_0000GBiN and 2024-08-08T18:14:21.000_0000GBrb, for which they will wait for the linking and confirmation from future, deep surveys. Ground-based follow-up images are available on request. Source data are provided with this paper.

Code availability

This work makes use of the following publicly available codes: NumPy[77], Matplotlib[78], Astropy[79,80], SciPy[81], Pandas[82,83], Astroquery[84] and Tycho Tracker (https://www.tycho-tracker.com/download).

53. Bradley, L. astropy/photutils: 1.8.0. *Zenodo* https://doi.org/10.5281/zenodo.7946442 (2023).
54. Parrott, D. Tycho tracker: a new tool to facilitate the discovery and recovery of asteroids using synthetic tracking and modern GPU hardware. *J. JAAVSO* **48**, 262 (2020).
55. Brown, M. E., Kulkarni, S. R. & Liggett, T. J. An analysis of the statistics of the Hubble Space Telescope Kuiper belt object search. *Astrophys. J. Lett.* **490**, L119–L122 (1997).
56. Cochran, A. L., Levison, H. F., Tamblyn, P., Stern, S. A. & Duncan, M. J. The calibration of the Hubble Space Telescope Kuiper belt object search: setting the record straight. *Astrophys. J. Lett.* **503**, L89–L93 (1998).
57. Hoffmann, T. et al. Debiasing astro-photometric observations with corrections using statistics (DePhOCUS). *Icarus* **426**, 116366 (2025).
58. Harris, A. W. A thermal model for near-Earth asteroids. *Icarus* **131**, 291–301 (1998).
59. Masiero, J. R. et al. Main belt asteroids with WISE/NEOWISE. I. Preliminary albedos and diameters. *Astrophys. J.* **741**, 68 (2011).
60. Alí-Lagoa, V. & Delbo, M. Sizes and albedos of Mars-crossing asteroids from WISE/NEOWISE data. *Astron. Astrophys.* **603**, A55 (2017).
61. Alí-Lagoa, V., Müller, T. G., Usui, F. & Hasegawa, S. The AKARI IRC asteroid flux catalogue: updated diameters and albedos. *Astron. Astrophys.* **612**, A85 (2018).
62. Wolters, S. D., Green, S. F., McBride, N. & Davies, J. K. Thermal infrared and optical observations of four near-Earth asteroids. *Icarus* **193**, 535–552 (2008).
63. Mainzer, A. et al. NEOWISE observations of near-Earth objects: preliminary results. *Astrophys. J.* **743**, 156 (2011).
64. Grav, T. et al. WISE/NEOWISE observations of the Hilda population: preliminary results. *Astrophys. J.* **744**, 197 (2012).
65. Vilenius, E. et al. "TNOs are Cool": a survey of the trans-Neptunian region. VI. Herschel/PACS observations and thermal modeling of 19 classical Kuiper belt objects. *Astron. Astrophys.* **541**, A94 (2012).
66. Pravec, P. & Harris, A. W. Fast and slow rotation of asteroids. *Icarus* **148**, 12–20 (2000).
67. Lebofsky, L. A. & Spencer, J. R. in *Asteroids II* (eds Binzel, R. P. et al.) 128–147 (Univ. Arizona Press, 1989).
68. Harris, A. W. & Lagerros, J. S. V. in *Asteroids III* (eds Bottke, W. F. Jr et al.) 205–218 (Univ. Arizona Press, 2002).
69. Mainzer, A. et al. The population of tiny near-Earth objects observed by NEOWISE. *Astrophys. J.* **784**, 110 (2014).
70. Fenucci, M., Novaković, B. & Marčeta, D. The low surface thermal inertia of the rapidly rotating near-Earth asteroid 2016 GE1. *Astron. Astrophys.* **675**, A134 (2023).
71. DeMeo, F. E. & Carry, B. Solar System evolution from compositional mapping of the asteroid belt. *Nature* **505**, 629–634 (2014).
72. Burdanov, A. Y. et al. SPECULOOS Northern Observatory: searching for red worlds in the northern skies. *Publ. Astron. Soc. Pac.* **134**, 105001 (2022).
73. Delrez, L. et al. SPECULOOS: a network of robotic telescopes to hunt for terrestrial planets around the nearest ultracool dwarfs. *Proc. SPIE* **10700**, 446–466 (2018).
74. Jehin, E. et al. Trappist: transiting planets and planetesimals small telescope. *Messenger* **145**, 2–6 (2011).
75. Mommert, M. PHOTOMETRYPIPELINE: an automated pipeline for calibrated photometry. *Astron Comput.* **18**, 47–53 (2017).
76. Levine, S. E. et al. Status and performance of the Discovery Channel Telescope during commissioning. *Proc. SPIE* **8444**, 430–444 (2012).
77. Harris, C. R. et al. Array programming with NumPy. *Nature* **585**, 357–362 (2020).
78. Hunter, J. D. Matplotlib: a 2D graphics environment. *Comput. Sci. Eng.* **9**, 90–95 (2007).
79. Astropy Collaboration et al. Astropy: a community Python package for astronomy. *Astron. Astrophys.* **558**, A33 (2013).
80. Astropy Collaboration et al. The Astropy Project: building an open-science project and status of the v2.0 core package. *Astron. J.* **156**, 123 (2018).
81. Virtanen, P. et al. SciPy 1.0: fundamental algorithms for scientific computing in Python. *Nat. Methods* **17**, 261–272 (2020).
82. The pandas development team. pandas-dev/pandas: Pandas. *Zenodo* https://doi.org/10.5281/zenodo.3509134 (2024).
83. McKinney, W. Data structures for statistical computing in Python. In *Proc. 9th Python in Science Conference* (eds van der Walt, S. & Millman, J.) 56–61 (SciPy, 2010).
84. Ginsburg, A. et al. astroquery: an astronomical web-querying package in Python. *Astron. J.* **157**, 98 (2019).
85. Christensen, E. J. et al. Status of the Catalina Sky Survey. In *Proc. Asteroids, Comets, Meteors Conference* 2587 (LPI Contributions, 2023).

Acknowledgements We thank P. Veres and M. Payne from the Minor Planet Center (MPC) for their support in enabling the processing of these JWST asteroid detections by the MPC. This work is based in part on observations made with the NASA/ESA/CSA JWST. The data were obtained from the Mikulski Archive for Space Telescopes (MAST) at the Space Telescope Science Institute (STScI), which is operated by the Association of Universities for Research in Astronomy, Inc., under NASA contract NAS 5-03127 for the JWST. These observations are associated with programmes 1177, 2304 and 3077, with T.P.G., L.K. and M.G. as principal investigators, respectively. A.Y.B. and J.d.W. thank M. J. Person for discussions about astrometry and S. Stuart for initial SFD calculations. J.d.W. and MIT gratefully acknowledge financial support from the Heising-Simons Foundation and C. Masson and P. A. Gilman for Artemis, the first telescope of the SPECULOOS network situated in Tenerife, Spain. This work has been supported by the Czech Science Foundation through grant 25-16507S (M.B.). This work has been supported by the NVIDIA Academic Hardware Grant Program. TRAPPIST is financed by the Belgian National Fund for Scientific Research (F.R.S.-FNRS) under grant PDR T.0120.21 and the University of Liège. E.J. is a Belgian FNRS Senior Research Associate. T.H. gratefully acknowledges the financial and technical support from the ESA, the Erasmus+ programme, co-funded by the European Union and the Cusanuswerk Bischöfliche Studienförderung, funded by the German Federal Ministry of Education and Research.

Author contributions A.Y.B. and J.d.W. designed and led the study. A.Y.B. performed the data reduction and asteroid detection (including injection-retrieval tests) following ref. 18 with support from J.d.W. J.d.W. designed the population-based distance estimation with support from A.Y.B., provided the preliminary size estimations and performed the information-content analysis for the size–frequency distribution with support from M.B. M.B. performed the interpretation of the size–frequency distribution. T.G.M. derived the final size and albedo estimates. T.H. provided the debiased H magnitudes. E.J. collaborated the exoplanet team with asteroids experts and led the ground-based follow-up observations together with A.Y.B., M.F., W.M.G., T.K., N.M., A.T. and C.A.T. M.F. led the rotation-curve analysis. M.M. provided the detailed orbital estimations. D.P. and S.N.H. provided complementary target identifications, flux estimates and support for Tycho Tracker. R.P.B. contributed to the early interpretation of the results. E.D., L.K., M.G., T.P.G., P.-O.L. and S.Z. led the JWST observation programmes of TRAPPIST-1 behind these serendipitous asteroid detections. All authors contributed to the writing of the paper.

Competing interests The authors declare no competing interests.

Additional information

Supplementary information The online version contains supplementary material available at https://doi.org/10.1038/s41586-024-08480-z.

Correspondence and requests for materials should be addressed to Julien de Wit.

Peer review information *Nature* thanks Joseph Masiero and the other, anonymous, reviewer(s) for their contribution to the peer review of this work.

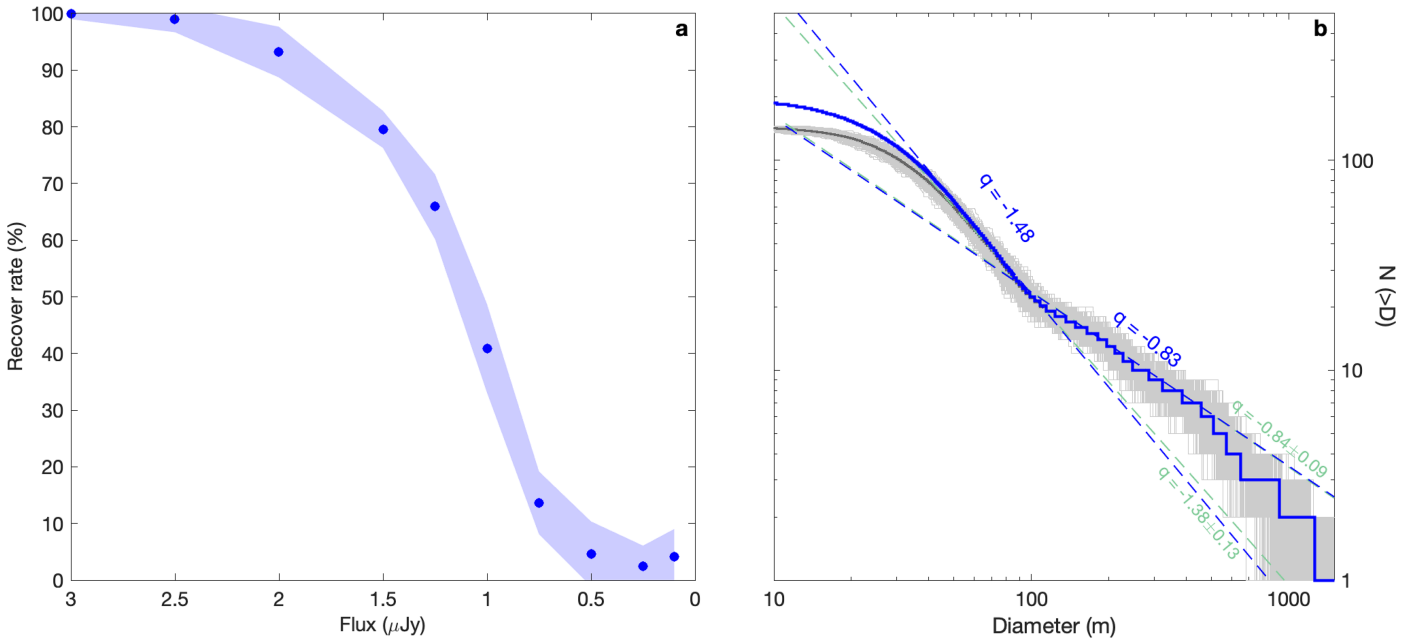

Extended Data Fig. 1 | Completeness test and recovery rate. a, Fraction of recovered synthetic asteroids as a function of their flux based on injection-recovery tests to assess the completeness of our search and correct the derived SFD. The shaded area represent the 1σ deviation from the reported rates seen across a range of injections. The derived cutoff is 0.5 μJy, with an observation bias starting at about 1.5 μJy (that is, at the 20–40-m size regime). **b**, Ensemble of cumulative SFDs built from 1,000 perturbed asteroid diameters to propagate the size uncertainties onto the SFD estimate (median in grey) by means of the Monte Carlo method[52], together with the SFD debiased for brightness-dependent recovery rate (blue).

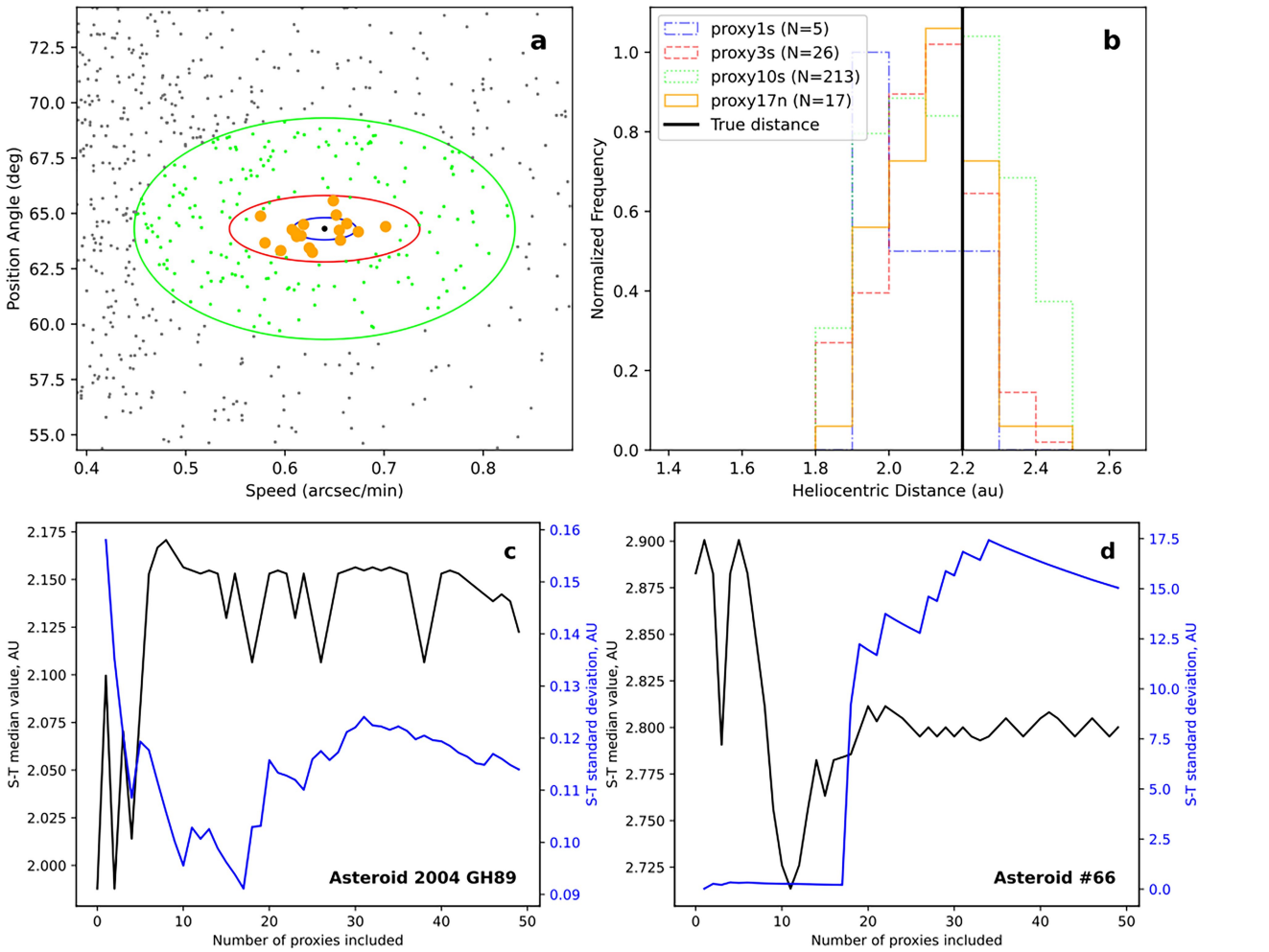

Extended Data Fig. 2 | Proof-of-concept application of population-based estimation of a distance to an asteroid. a, Speed (v) and position angle (PA) of asteroid 2004 GH89 (black dot) compared with an ensemble of other known asteroids close to the FoV at the time of the observation (grey dots), together with proxy1s, proxy3s and proxy10s ellipses (blue, red and green, respectively) used to select neighbours/proxies and the final 17 proxy17n proxies used (orange). **b**, Histogram of heliocentric distances (S–T) from the different ensembles of proxies compared with the true value (black line), confirming that, with an increasing number of proxies (N), the derived orbital configuration converges towards truth. **c**, Estimated heliocentric distance (black) and its uncertainty (blue) for asteroid 2004 GH89 as a function of N. For $N \ll 10$, small-number statistics can bias the derived distance and yield an artificially large associated uncertainty. Beyond $N \approx 20$–25, more proxies present new/different orbital configurations, resulting in sudden changes in the estimated value (otherwise converging) and thus a progressive inflation of the estimated uncertainty. **d**, Same as **c** but for unknown asteroid #66 (probably NEO) with a limited number of close proxies, leading to its 19th and 20th closest proxies to be clear outliers (trans-Neptunian objects) resulting in a sudden jump of its derived uncertainty.

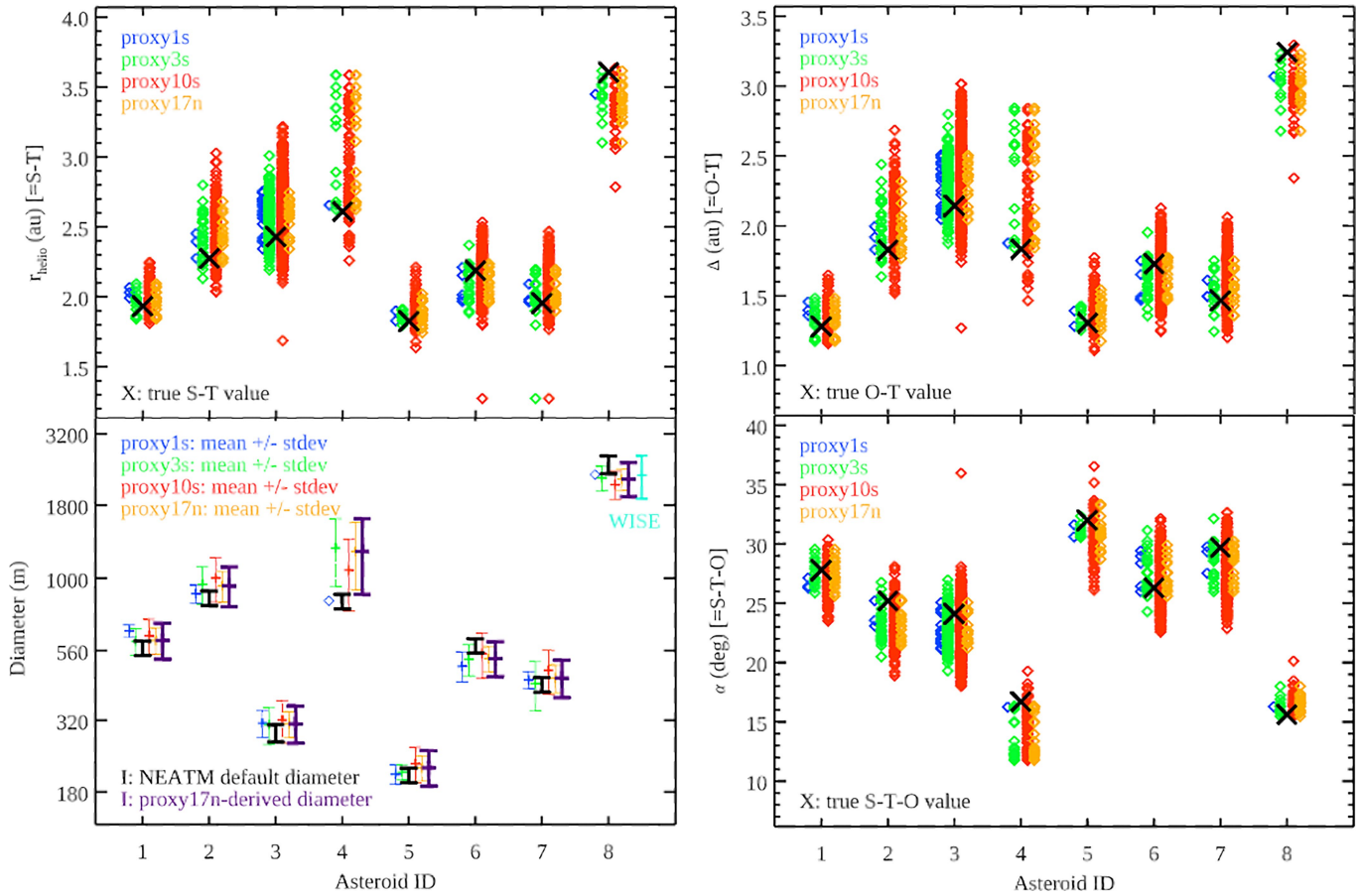

Extended Data Fig. 3 | Proof-of-concept application of the population-based orbit derivation for the eight known asteroids. Left, derived heliocentric distance for the eight known asteroids based on the proxy1s, proxy3s, proxy10s and proxy17n neighbours (blue, green, red and orange, respectively) and the same for the radiometric diameter inferred from the population-based heliocentric distance versus true orbit. Asteroid #8 has a measured size, reported in cyan. Right, derived distance from JWST to the eight known asteroids and corresponding S–T–O phase angles. For all proxy3s, proxy10s and proxy17n estimates for the distances—which are based on a large enough (that is, statistically relevant) number of proxies—the existing size and phase angles agree to within 1σ, supporting the reliability of the methodology used. See asteroid names in Extended Data Table 1, in which they are reported in the same order (that is, asteroid #1 is 2011 SG255 and asteroid #8 is (472944) 2015 GH28).

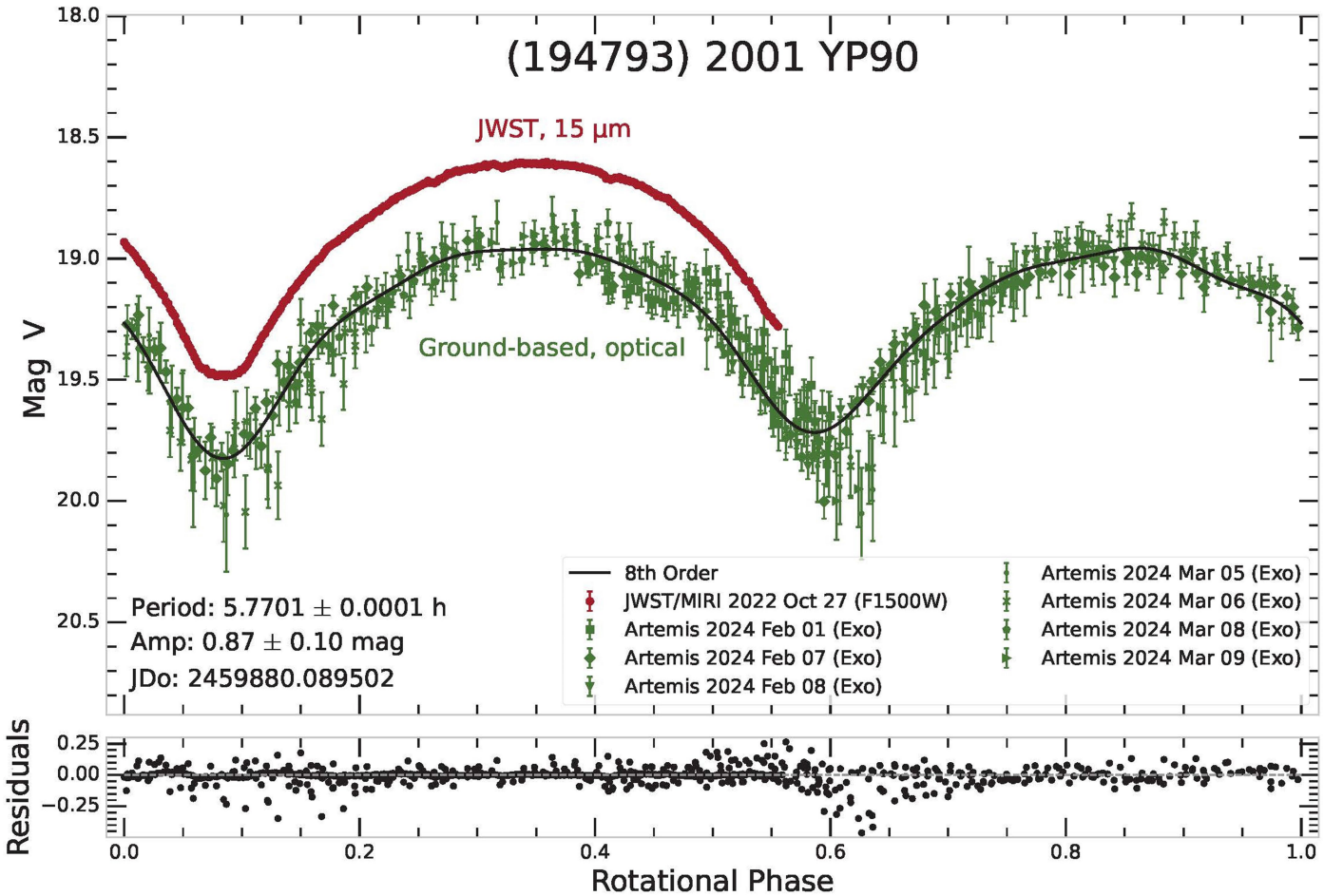

Extended Data Fig. 4 | Phased rotational light curve of 2001 YP90. Photometric observations of 2001 YP90 obtained with the Artemis telescope[72] (in green) indicate a rotation period of 5.7701 ± 0.0001 h and an amplitude of 0.87 ± 0.10 mag. The red curve corresponds to the MIRI observations shifted to the V-band data (−0.35 mag for clarity) and shows a very good match with the optical observations in shape and amplitude. The MIRI data uncertainties are plotted but are smaller than the markers size.

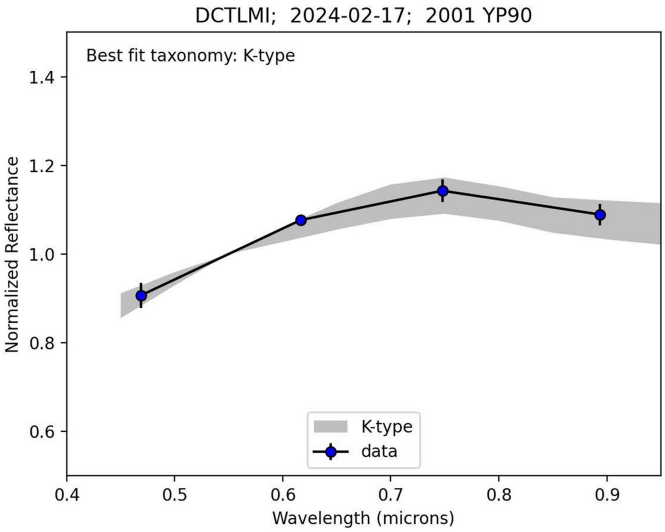

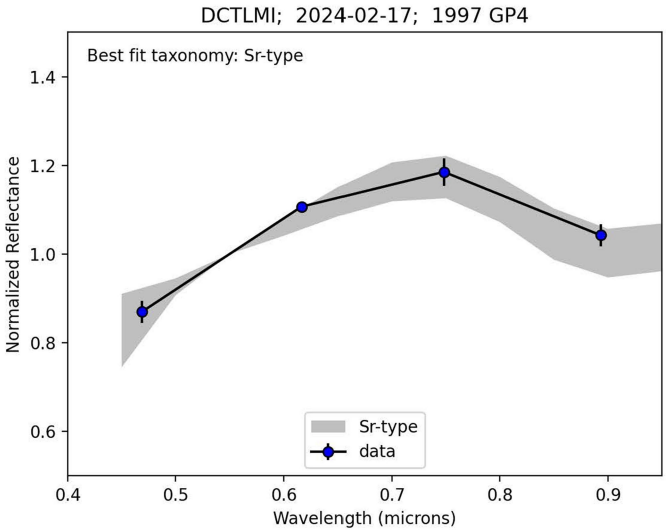

Extended Data Fig. 5 | Spectro-photometric taxonomic types of bright asteroids 2001 YP90 and 1997 GP4. Data were obtained with SDSS griz filters. Best-fit taxonomic types were determined on the basis of minimizing r.m.s. residuals between the data and resampled templates of taxonomic types in the Bus–DeMeo system. The albedos inferred from our radiometric analysis are in agreement with those from taxonomic classifications.

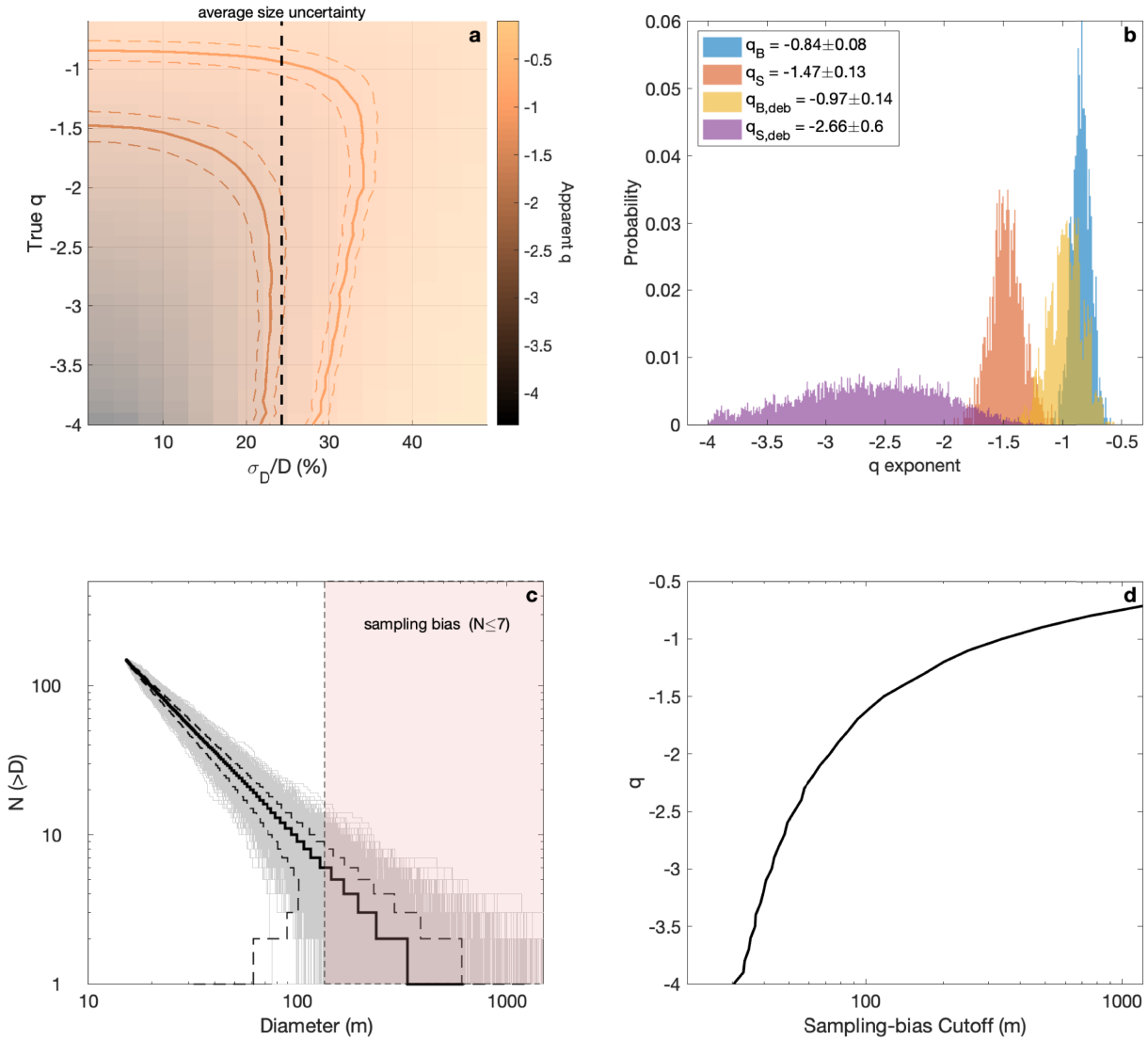

Extended Data Fig. 6 | Information content and sensitivity analysis of a SFD. a, True versus apparent q exponent for ensembles of 1,000 samples of 150 asteroids drawn from a synthetic family, as a function of the relative size uncertainty (σ_D/D). Apparent slopes are consistently shallower as 'smoothed out' by size measurements following primarily a Gaussian distribution. The contours represent the $q_S = -1.47$ and $q_B = -0.84$ slopes observed, which match true/debiased slopes of $q_{S,deb} \approx -2.66$ and $q_{B,deb} \approx -0.97$ for our average size uncertainty (dashed line). **b**, Posterior probability distributions for the observed q exponents in the small-size and big-size regimes (q_S and q_B, respectively, below and above the transition at about 100 m) and their debiased estimates ($q_{S,deb}$ and $q_{B,deb}$, respectively). **c**, SFDs from 3,000 random draws of 150 asteroids from a $q = -1.45$ population of about 1×10^6 asteroids showing consistent slopes until about 130 m, owing to small-number statistics ($N \leq 7$), the 'sampling-bias cutoff'. **d**, Relationship between the sampling-bias size cutoff and the q coefficient of a population for a sample size of 150 asteroids.

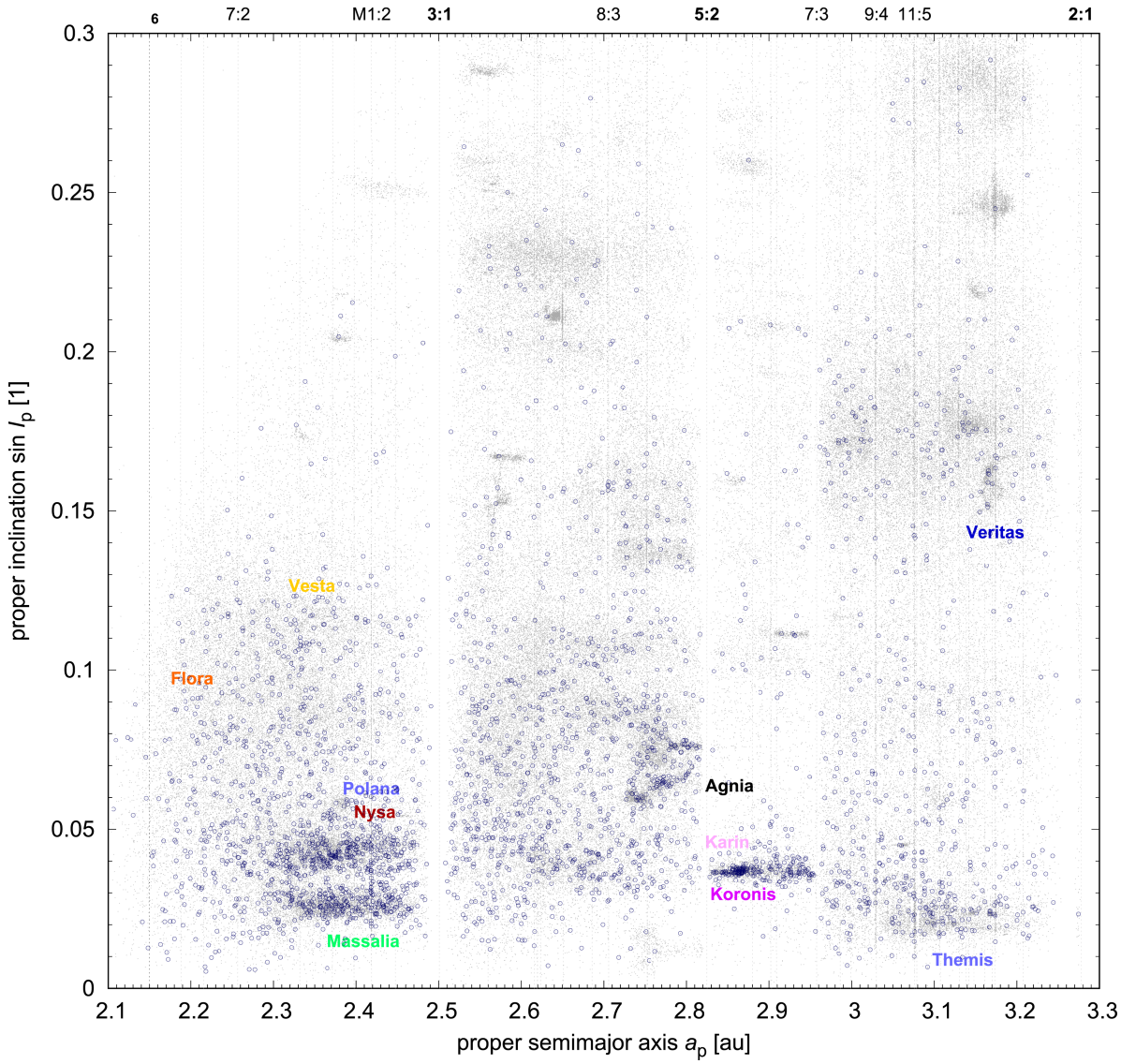

Extended Data Fig. 7 | Orbital elements of known asteroids located close to the field of TRAPPIST-1. All of these asteroids had a similar speed and position angle as the unknown asteroids observed by JWST. Their proper semimajor axis a_p versus the proper inclination $\sin i_p$ (blue circles) is compared with other faint MBAs observed by the Catalina Sky Survey[85] (grey dots). Their concentrations ('clouds') correspond to known asteroid families[19]. Sampling is non-random owing to the geometry of JWST observations. Preferentially, the Nysa, Polana and Massalia families are sampled, together with other families at low inclinations (Koronis2 and Karin).

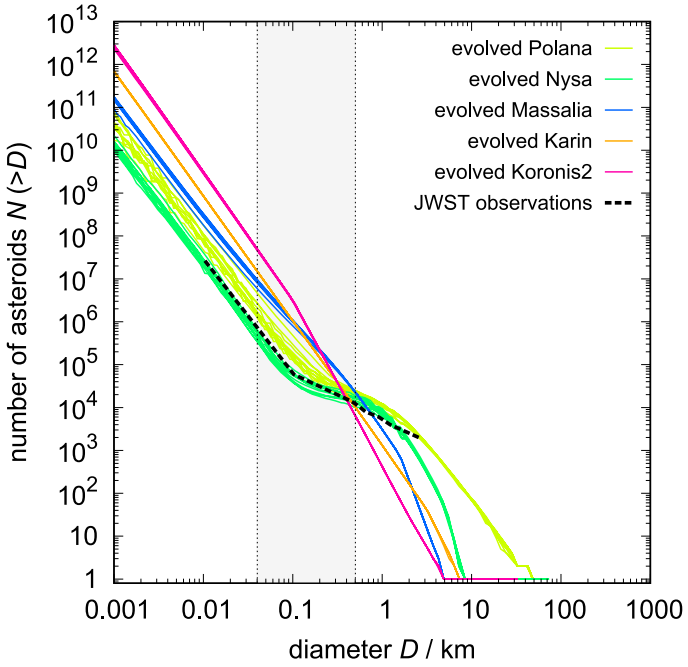

Extended Data Fig. 8 | Young and old asteroid families have very different SFDs between 1,000 and 50 m. A comparison of synthetic distributions of asteroid families from refs. 13,14,31 shows that prominent young families (Massalia, Koronis2 and Karin) commonly have a steep slope (the exponent $q \simeq -2.5$ up to -4.0), whereas old families (Polana and Nysa) have a shallow slope ($q \simeq -1.0$ to -1.5). This difference results from the fact that hundred-metre-sized bodies are the weakest bodies in terms of their strength (that is, energy per unit of mass needed for disruption)[30]. Consequently, their collisional evolution is so great that, after approximately 100 Myr, the exponent changes substantially[13].

Extended Data Table 1 | Properties of the eight known asteroids

Name	H_{fit} (*)	R_{helio} (au)	Δ(au)	α	η(**)	flux(μJy)(***)	D (m)	p_v
2011 SG255	19.28	1.9328	1.2798	27.8	1.01	1,660±100	571±33	$0.105^{+0.034}_{0.027}$
(152630) 1997 GP4	17.09	2.2750	1.8284	25.2	0.99	1,240±74	854±50	$0.353^{+0.099}_{0.084}$
2021 FR9	19.32	2.4289	2.1444	24.1	0.98	90±9	289±20	$0.395^{+0.108}_{0.092}$
(194793) 2001 YP90	17.32	2.6092	1.8337	16.7	0.91	1,030±62	832±49	$0.302^{+0.086}_{0.073}$
2013 PG137	20.37	1.8259	1.3056	32.0	1.05	200±12	206±12	$0.295^{+0.086}_{0.071}$
2004 GH89	18.15	2.1869	1.7275	26.3	1.00	710±43	583±34	$0.286^{+0.082}_{0.069}$
2016 UR72	18.83	1.9551	1.4658	29.7	1.03	620±37	426±25	$0.286^{+0.084}_{0.069}$
(472944) 2015 GH28	16.66	3.6049	3.2427	15.6	0.90	1,630±163	2,497±177	$0.061^{+0.020}_{0.015}$

H_{fit} reports the estimated V-band H magnitudes, R_{helio} the heliocentric distances, Δ the JWST-centric distance, α the phase angle, η the infrared beaming parameter, D the diameters and p_v the geometric V-band albedo. *We assume a ±0.3 mag error for the radiometric size–albedo calculation. **The η values were calculated by means of the η relation given above[61], but we allow for a ±10% uncertainty (which translates into an extra 5% uncertainty in the diameter calculation and an extra 10% in the albedo calculation). The calculated minimum (maximum) η values for the eight asteroids are 0.81 (1.15). ***The detections of the known asteroids all have very high SNRs, but for the size–albedo determination, we took an absolute flux error of 6%, covering the MIRI imaging flux calibration, colour corrections (between the stellar and the asteroid spectral energy distribution) and MIRI signal drift uncertainties. For the asteroids #03 (flux below 100 μJy) and #08 (located in the coronagraphic part of the MIRI detector), we increased the flux error to 10%.

Extended Data Table 2 | Probable associations of 138 unknown asteroids detected by the JWST to individual populations

ID	Family	ID	Family	ID	Family
1	Themis?	51	Nysa	101	
2		52	high-inclination	102	Nysa, Massalia, Karin
3		53	Nysa, Polana	103	Nysa, Massalia
4		54		104	Flora?
5		55		105	Flora
6		56		106	NEO?
7	high-inclination	57		107	Nysa, Massalia, Karin
8	Polana	58	Massalia?	108	Massalia, Nysa
9		59	NEO?	109	Themis
10	Nysa	60		110	Nysa?
11		61		111	Massalia, Nysa
12	Veritas	62	Nysa?	112	Massalia, Nysa
13	Nysa, Massalia	63		113	Massalia, Nysa
14	Nysa, Massalia, Karin	64		114	Nysa, Massalia, Polana, Karin
15	Nysa, Polana	65		115	Flora, Vesta?
16	NEO?	66		116	Massalia, Polana
17	Massalia, Themis	67		117	Nysa, Massalia, Polana, Karin
18	Themis?	68		118	Nysa, Massalia, Polana, Karin
19	Massalia	69	Massalia	119	Massalia, Nysa, Karin
20		70		120	Massalia?
21		71		121	Massalia?
22	Vesta?	72		122	Veritas?
23	Massalia, Nysa	73		123	Nysa, Massalia, Polana, Karin
24	Massalia	74		124	Massalia, Polana
25		75	Nysa?	125	Polana?
26	Veritas?	76		126	Flora?
27	Flora, Vesta	77	NEO?	127	Nysa, Massalia
28	Vesta?	78		128	Vesta?
29		79	Nysa, Massalia	129	Flora?
30	Veritas?	80	Hilda?	130	Massalia
31	Massalia, Nysa, Polana, Karin	81	Massalia?	131	Massalia
32	Veritas?	82	Veritas?	132	Nysa, Massalia, Polana
33	Massalia, Nysa, Polana, Karin	83	Massalia, Nysa, Polana, Karin	133	Vesta?
34		84	high-inclination	134	Vesta?
35	Themis	85	Massalia, Nysa	135	Agnia?
36		86	Massalia, Nysa, Polana, Karin	136	NEO?
37		87	Nysa, Massalia, Karin	137	Nysa, Massalia, Polana, Karin
38	Massalia, Nysa	88	Nysa, Massalia	138	Flora?
39		89	Polana?	139	Massalia, Nysa
40	NEO?	90			
41	Vesta?	91	Trojan		
42		92	Veritas?		
43		93	Veritas?		
44	Massalia, Nysa, Polana, Karin	94	high-inclination		
45	high-inclination	95	Massalia, Nysa		
46	Themis	96	Massalia, Nysa, Karin		
47		97	Nysa, Massalia, Karin		
48		98	Massalia, Nysa, Koronis		
49		99	Flora		
50		100	high-inclination		

According to the measured proper motions and position angles, most of them belong to main-belt families and only a few to NEOs, Hildas and trojans.